A druggable redox switch on SHP1 controls macrophage inflammation

Mei Ying Ng[1,2,*], Meredith N. Nix[3,4,*], Guangyan Du[3], Ivan Davidek[3], Nils Burger[1,2], Sanghee Shin[1,2], Sean Toenjes[3], Haopeng Xiao[1,2], Shelley Wei[1,2], Hyuk-Soo Seo[1,5], Sirano Dhe-Paganon[1,5], Thomas E. Wales[6], John R. Engen[6], Evanna L. Mills[7,8], Jianwei Che[1,#], Tinghu Zhang[3,#], Nathanael S. Gray[3,#], & Edward T. Chouchani[1,2,9,#]

[1]Department of Cancer Biology, Dana-Farber Cancer Institute, Boston, MA, USA.
[2]Department of Cell Biology, Harvard Medical School, Boston, MA, USA.
[3]Department of Chemical and Systems Biology, CHEM-H and SCI, Stanford Medical School, Stanford University, Stanford, CA, USA.
[4]Department of Chemistry, Stanford University, Stanford, CA, USA.
[5]Department of Systems Biology, Harvard Medical School, Boston, MA, USA.
[6]Department of Chemistry and Chemical Biology, Northeastern University, 360 Huntington Avenue, Boston, MA 02115, USA.
[7]Department of Cancer Immunology and Virology, Dana-Farber Cancer Institute, Boston, MA, USA.
[8]Department of Immunology, Harvard Medical School, Boston, MA, USA
[9]Howard Hughes Medical Institute, Chevy Chase, MD, USA.
*These authors contributed equally: Mei Ying Ng, Meredith N. Nix.
[#]Corresponding authors: jianwei_che@dfci.harvard.edu, ztinghu8@stanford.edu, nsgray01@stanford.edu, edwardt_chouchani@dfci.harvard.edu

Abstract

Immunological proteins are major disease targets, and the majority remain undrugged. Post-translational redox modification of protein cysteine residues has emerged as a mode of immune cell regulation, especially in the context of the macrophage cytokine response[1,2]. Here, we develop a strategy for systematic discovery and small molecule functionalization of redox regulated cysteines on immunological proteins. Using deep redox proteomics, we annotate 788 cysteines across diverse functional domains of immune-relevant proteins that are redox regulated *in vivo*. We demonstrate how these sites can be leveraged to develop cysteine-directed pharmacology, exemplified by a newfound cysteine activation site on the core immunological regulator SHP1. By targeting Cys102 on SHP1, we develop a highly selective covalent SHP1 agonist, SCA. SCA binding to Cys102 in the N-terminal Src Homology 2 (N-SH2) domain promotes its rearrangement to relieve auto-inhibition and drive SHP1 activation. In mouse and human macrophages, SCA and its analogues rapidly and selectively engage SHP1 Cys102 and antagonize interleukin-1 receptor-associated kinase signaling and lipopolysaccharide (LPS)-induced pro-inflammatory cytokine production. Together, we discover a druggable cysteine redox switch controlling the macrophage cytokine response, and provide a compendium of functionally annotated redox regulated sites for cysteine-directed therapeutics development.

Introduction

A wide range of immunological processes are regulated through the generation of reactive oxygen species (ROS) and related redox-active molecules[2-5]. Redox-active metabolites regulate immune cells through covalent modification of protein cysteine residues, consequently modifying protein function[2-4,6]. These redox modifications occur due to the distinct reactivity of protein cysteines compared to other amino acids, rendering them selective targets for this form of post-translational modification. A prominent example of this type of regulation is found in the context of macrophage cytokine production. Oxidation of protein cysteines by ROS regulates production of pro-inflammatory cytokines by macrophages[5-8]. Conversely, covalent modification of distinct protein cysteines by other redox active metabolites inhibits pro-inflammatory cytokine production and drives an anti-inflammatory phenotype[6,9-11]. Despite the widespread importance of protein cysteine redox regulation over immune cell function, there has been a persistent lack of rigorous information regarding the specific protein modifications that explain the molecular basis for these processes. Elucidating the cysteine targets

on immunological proteins that regulate their function is fundamental for understanding the mechanistic basis for redox regulation of the immune system.

In addition, a more complete understanding of redox regulated cysteine sites on immune targets could provide a foundation for systematic therapeutic targeting of the immunological proteome. Indeed, the intrinsic reactivity of redox regulated cysteines can be harnessed for the development of covalent tool compounds and drugs[12,13]. In clinical oncology, numerous individual redox-active cysteines have been targeted therapeutically using electrophilic small molecules, aiming to inhibit protein activity or interfere with protein-protein interactions[12]. The effectiveness of these strategies has demonstrated the potential for design of electrophilic molecules to selectively modify specific protein cysteines.

In this work, we develop a strategy for discovery and small molecule functionalization of *in vivo* redox regulated cysteines on immunological proteins. Using deep redox proteomics, we annotate cysteines across diverse functional domains of 1,125 immune-relevant proteins to identify those that are redox regulated *in vivo*. We demonstrate how this redox regulated cysteine landscape can be queried with high-throughput chemical biology to manipulate the function of immunological proteins that previously were pharmacologically challenging, particularly in the development of positive allosteric modulators of protein phosphatases for which there are few successful examples. We develop a selective covalent agonist of the central immune regulator SHP1, which functions by targeting a redox regulated cysteine that relieves intrinsic auto-inhibition. This previously unknown mechanism of SHP1 activation inhibits pro-inflammatory cytokine production and inflammation in macrophages. We provide a compendium of redox regulated cysteines across the immunological proteome (provided as an online resource at https://chouchani-lab.shinyapps.io/oximmune/) as a roadmap to engineer pharmacological regulators of currently undrugged immune-relevant proteins.

Results

Systematic discovery of *in vivo* redox regulated cysteines on immunological proteins. Despite the central importance of protein cysteine redox regulation in immunology, a comprehensive understanding of the specific modifications that underlie these processes is lacking. Because cysteines are relatively rare within proteins, and cysteine redox modifications are chemically labile, they are technically challenging to determine proteome-wide. Moreover, to identify functional nodes through which ROS and related species exert their physiological roles, it is important to quantify the stoichiometry of reversible modification on a particular cysteine residue. Sites subject to dynamic modification, with the capacity to exhibit large absolute changes in modification state, represent a core property of redox regulated cysteines[14-16]. Quantifying these regulated sites *in vivo* is a particular challenge for immunological proteins, which exhibit low abundance in tissues.

To address these challenges, we recently developed Oximouse, a quantitative and comprehensive characterization of protein cysteine oxidation *in vivo*. This technology makes use of cysteine derivatization and enrichment chemistry to determine % redox modification of ~171,000 protein cysteines sites across ten tissues in mice[14]. Here, we evolved this compendium to explore the biological role of individual redox regulated protein cysteines across the immunological proteome *in vivo*, and in doing so we develop a resource called OxImmune. We defined the immunological proteome to include all proteins contained in InnateDB. InnateDB is comprised of 1,125 proteins with experimentally verified roles in the innate immune response[17]. To profile redox regulation across this immunological proteome *in vivo*, we examined the redox modification state of ~34,000 unique cysteines in living mouse tissues **(Figure 1a)**. From this population, we focused our analysis to 13,018 cysteines on InnateDB proteins conserved between mouse and human **(Figure 1a & Supplementary Table 1)**. For each cysteine residue, OxImmune tracks the modification state across 10 tissues and two ages. It is appreciated that the local tissue environment exerts widely divergent effects on immunological proteins and processes. On this basis, we hypothesized that by tracking the natural heterogeneity of cysteine modification state inherent to different tissue environments, we could reveal cysteine sites subject to dynamic modification that depends on local milieu.

We tracked % modification of each protein cysteine under multiple tissue conditions to define each site based on capacity for dynamic modification **(Figure 1b)**. We categorized each mapped cysteine across the immunological proteome as follows:

i) Stable redox state – a cysteine never exhibiting more than 10% difference in redox modification status between any two tissue conditions.
ii) Dynamic redox state – a cysteine exhibiting more than 10% difference in redox modification status between any two tissue conditions.

From this analysis, ~6% (830) of all mapped cysteines on immunological proteins were defined as dynamically redox regulated across tissues *in vivo* **(Figure 1b)**. Dynamic endogenous redox modification often marks regulatory sites on target proteins[14,18], so we next classified these residues across the immunological proteome. Redox regulated cysteines were found on a wide range of protein families, including kinases, transcription factors, phosphatases, and metabolic enzymes **(Figure 1c-f)**. Across all families, ~95% (788) of regulated cysteines mapped to established functional domains within the protein, including enzyme active sites, allosteric regulatory sites, nucleotide binding regions, and protein-protein interaction sites **(Figure 1g & Supplementary Table 1)**. We mapped redox regulated cysteines onto these domains, as well as experimentally determined structures across the immunological proteome, which enabled mechanistic prediction of the consequence of cysteine modification for each site **(Figure 1h & Supplementary Table 1)**. Among the most prominently redox regulated enzyme active sites were caspases, which are known to frequently feature redox modified active site cysteines[19,20]. Notably, several of these cysteine targets have been targeted previously by covalent caspase inhibitors[21-25], underpinning the potential of targeting this class of regulatory cysteines. Likewise, protein tyrosine and serine/threonine kinases are known to be redox regulated and exhibit important regulatory action on immune processes[26-29]. Many members of this enzyme class contain cysteines subject to dynamic oxidation *in vivo*, both in active and allosteric sites **(Figure 1h & Supplementary Table 1)**. This was also found to apply to phosphatases, exemplified by the catalytic domain of protein phosphatase 1 **(Figure 1h & Supplementary Table 1)**[30-32]. Beyond these examples, many other protein classes such as proteases, and central components of immune relevant signaling cascades, contain dynamically oxidized cysteines **(Supplementary Table 1)**. Together, structural and domain annotation of the redox regulated immunological proteome identified 788 instances of regulatory cysteines on established functional domains of major immune regulatory proteins **(Figure 1h)**. We provide this dataset, including target class and domain and structural annotations, via an online interface, which we use as a basis to better understand the biological role of redox regulation of immunological proteins (https://chouchani-lab.shinyapps.io/oximmune/).

Chemical manipulation of immunological proteins by targeting redox regulated cysteines. By uncovering hundreds of protein cysteines that are subject to oxidative modification *in vivo* **(Figure 1),** we reasoned that this provides an opportunity to leverage these same sites for therapeutic manipulation. The high nucleophilicity and redox activity that render cysteines amenable to dynamic oxidative modification allows for selective targeting by small molecules containing an appropriately oriented electrophilic warhead. It is now well appreciated that solvent-accessible, nucleophilic cysteine thiolates can be selectively targeted by small molecule electrophiles[13,33,34]. Based on this rationale, we explored whether redox regulated cysteines identified in OxImmune could be exploited for pharmacological targeting of central immunological processes.

We focused our attention to protein classes that have been challenging to target pharmacologically. A prominent example of this is found in protein phosphatases, which are central to immune cell function, and for which positive allosteric modulators have been extremely challenging to develop. This is exemplified by the SH2 domain containing protein tyrosine phosphatase-1 (SHP1) **(Figure 2a)**. SHP1 is a core inhibitor of autoimmunity[35]. SHP1 activation is central to inhibition of macrophage, monocyte, and T cell-driven inflammation[35,36]. Mice deficient for SHP1 suffer from microbe-driven inflammation and spontaneous autoimmunity[37]. T cells from patients with rheumatoid arthritis show tonic inhibition of SHP1[38], while active SHP1 appears to be required for the anti-inflammatory action of IFNβ in multiple sclerosis[39,40]. Moreover, transgenic SHP1 overexpression protects mice from inflammatory arthritis without noticeable adverse effects[41]. In the context of a pro-inflammatory stimulus,

activated SHP1 directly binds to interleukin-1 receptor-associated kinase 1 (IRAK1) and antagonizes IRAK1-mediated NF-κB signaling[42,43]. SHP1 activity is known to be suppressed by auto-inhibition, whereby the N-SH2 domain blocks access of substrate to the active site[44].

Analysis of OxImmune identified redox regulated Cys102 that exists in an N-SH2 proximal pocket involved in the structural rearrangement of SHP1 from an auto-inhibited state to an active conformation[44] **(Figure 2a,b)**. On this basis, we hypothesized that modification of SHP1 Cys102 could drive a conformational change to the N-SH2 domain leading to elevation of phosphatase activity. To test this, we set out to discover selective cysteine-targeted ligands of SHP1 Cys102. We applied deep cysteine chemoproteomic mapping (CPT-MS)[14] of human THP-1 monocyte derived macrophages (MDM) and mouse immortalized bone marrow derived macrophages (iBMDM) to query the cysteine proteome under native conditions for engagement with cysteine-reactive small molecules. CPT-MS makes use of cysteine-reactive phosphate tags (CPTs) that facilitate enrichment of cysteine-containing peptides using metal affinity chromatography, allowing for deep mapping of the cysteine proteome[14,45,46]. CPT-MS quantified small-molecule engagement with ~20,000 unique cysteines in a single experiment **(Figure 2c & Supplementary Table 2,3)**. Using CPT-MS, we screened for small molecules that could selectively engage SHP1 Cys102 in human THP-1 MDMs and mouse iBMDMs. We identified a molecule, henceforth referred to as SCA1, that covalently modified SHP1 Cys102 **(Figure 2d & Extended Data Figure 1a)**. SCA1 exhibited a very high degree of proteome-wide selectivity for SHP1 Cys102 at low micromolar concentrations. Between 5-40 μM, SCA1 reproducibly and selectively labelled SHP1 Cys102 in THP-1 MDMs **(Figure 2e & Supplementary Table 3)** and iBMDMs **(Extended Data Figure 1a & Supplementary Table 2)**. At these concentrations, SCA1 did not reproducibly label other cysteine sites with higher stoichiometry compared to SHP1 Cys102, with the exception of DHX40 Cys153 that was non-specifically engaged at higher concentrations. More generally, these data indicated a near complete lack of reproducible off-target engagement of the observable cysteine proteome **(Figure 2e, Extended Data Figure 1a & Supplementary Table 2,3)**. SCA1 engagement of SHP1 Cys102 in THP-1 MDMs and iBMDMs was concentration dependent and readily achieved above 50% stoichiometry between 10-20 μM **(Figure 2f & Extended Data Figure 1b)**, and exhibited high selectivity compared to the closely related PTP SHP2 **(Figure 2g,h & Extended Data Figure 1c,d)**.

We confirmed direct labeling of Cys102 by SCA1 by examining the intact mass of recombinant human SHP1. Incubation of SHP1 with 5 or 10 molar equivalents of SCA1 resulted in a mass shift of the protein corresponding to the mass of a SCA1 adduct **(Figure 3a)**. Peptide analysis of recombinant SHP1 determined that this labeling was attributable to covalent modification of Cys102 **(Figure 3b)**. Moreover, covalent modification of SHP1 by SCA1 was completely lost upon mutagenesis of SHP1 Cys102 to serine **(Figure 3c)**. We additionally confirmed labeling of SHP1 by SCA1 in iBMDMs and THP-1 MDMs by generating a biotin-conjugated SCA1 analog (biotinylated SCA1), which we established could also label SHP1 **(Figure 3d)**. Cells were lysed and incubated with biotinylated SCA1 followed by biotin enrichment, which demonstrated robust enrichment for SHP1 at as low as 1 μM biotinylated SCA1 **(Figure 3d)**. Conversely, pre-treatment of cells with titrated SCA1 followed by 10 μM biotinylated SCA1 demonstrated that biotin enrichment of SHP1 could be fully competed by SCA1 **(Figure 3e)**. Taken together, these data uncover SCA1 as a selective electrophile targeting Cys102 of SHP1 *in vitro* and in mouse and human macrophages.

Structural models for SCA1-mediated modification of SHP1. To understand how SCA1 binds to SHP1 and consequently could modulate its function, we used a combination of covalent docking and molecular dynamics simulations to study its interactions with Cys102 and the surrounding residues. There are two distinct conformations of full length SHP1 reported, corresponding to the auto-inhibited (PDB ID: 2B3O) and active (PDB ID: 3PS5) form, respectively[44]. SHP1 activation requires N-SH2 dissociation from the active site[44]. Cys102 is located at the hinge connecting N-SH2 and C-SH2 domains. Through covalent docking and subsequent 1 μs molecular dynamics simulations, the proposed binding mode of SCA1 in the active form of SHP1 revealed strong cation-π interactions between the SCA1 phenyl ring and SHP1 Arg7 during most of the simulation time **(Figure 4a)**. In addition, a weaker but still significant edge-to-π interaction between the pyrazolo[1,5-a]pyrimidine ring and Phe39 persisted in 37% of the simulation length. One of the most important interactions for SCA1 is the

hydrogen bond between the amine of the acrylamide and Phe5 backbone. This hydrogen bond persisted almost throughout the entire simulation, indicating its critical role. This model predicts that this interaction could effectively couple the N-terminal tail with the C-SH2 domain, which would be predicted to stabilize the active conformation, or facilitate the transition from inactive to active state by promoting the concerted motion of the two SH2 domains. The binding mode also showed limited space between the Cl atom and His114, Leu139 and Met1, and solvent exposure of the meta position of the phenyl ring, suggesting opportunities for further modification and chemical optimization of SCA1. The binding pocket is formed primarily by residues in β strands in the two SH2 domains and the loops between them, such as Arg3 to Arg7, Pro31, Ser32, Phe39, and His114 **(Figure 4a)**. In comparison with apo active state SHP1 simulation, residues from 209 to 219 became much more flexible with SCA1 bound, even though they are not in direct contact with the compound, presumably due to structural rearrangements of the internal loop in C-SH2 domain to accommodate compound binding.

Optimization of SCA1 to enhance engagement with SHP1. Using the SHP1-SCA1 docking model as a guide, we next explored the tolerability of the SCA1 scaffold to modification to enhance SHP1 binding **(Figure 4b-d)**. The binding model of SCA1 with SHP1 revealed solvent exposure at the 5th-position of the phenyl ring that facilitates tolerability to modifications, while considerable space rigidity and constraint at the 5th-position of the pyrazolo[1,5-a]pyrimidine core limits amenability to modification **(Figure 4a)**. On this basis, we set out on a medicinal chemistry campaign to improve SHP1 conjugation by derivatizing SCA1. First, we fixed the R2 group with chloride at the 5th-position and then screened synthesized aniline-containing analogs that bear an acrylamide warhead. As shown in **Figure 4b**, the para-regioisomer (SCA2) becomes incapable of labeling, likely owing to an incompatible trajectory of the warhead to Cys102 as suggested by the binding model **(Figure 4a)**. Similarly, the model indicated that modifications to the ortho (SCA3) and para (SCA4) positions could significantly alter the phenyl orientation due to steric repulsion with the core, resulting in loss of SHP1 conjugation **(Figure 4b)**. In contrast, modifications to the meta position including the installation of a methyl (SCA5), methoxy (SCA6), or bromo (SCA7) group retained SHP1 labeling as predicted by the model, with the bromo group further enhancing labeling. Replacing aniline with a 3-pyridyl group resulted in a slight reduction in conjugation efficiency (SCA8). In contrast, replacing aniline with a 4-pyridyl group significantly improved labeling up to 100% under the same labeling conditions, indicating a potential polar interaction or improved cation-π interaction with SHP1 Arg7 (SCA9). Although thiophene, a phenyl bio-isostere, was used in the design, it did not demonstrate the formation of an adduct with SHP1 (SCA10), likely due to slight alteration in the warhead orientation preventing a Michael addition reaction. Similarly, rigidifying the warhead by cyclization resulted in complete loss of SHP1 conjugation (SCA11), further supporting the requirement of the hydrogen bond between amine of the acrylamide and Phe5 backbone in the model. In addition, we fixed the warhead and replaced Cl with H, NH_2, NMe_2 or OMe. As shown in **Figure 4b**, while H and NMe_2 (SCA12 and SCA14) completely abolished the conjugation with SHP1, NH_2 and OMe modifications (SCA13 and SCA15) retained 10% and 32% labeling respectively, consistent with a small hydrophobic cavity in this region. We also explored whether conjugation could be realized through an oxygen linker. However, compound SCA16 proved to be incompetent for conjugation, presumably due to electrostatic repulsion between the oxygen and carbonyl of Pro142. Adding a methylene dimethyl amine to the terminal end of the warhead also blocked the warhead's proximity to Cys102, likely as a result of steric hindrance or incompatible electrostatic environment due to multiple positively charged residues residing in the pocket (SCA17).

We next advanced SCA9 as a new lead compound and conducted a focused structure-activity relationship (SAR) study around the pyridine ring. Installing a polar group to the ortho position of the nitrogen pyridine reduced SHP1 conjugation by SCA18, SCA19 and SCA20 that bear an amino, cyclopropane amine, and aniline group respectively (**Figure 4c**). This was also observed by the installation of a methoxy group in SCA21, and of extended polar groups in SCA22, SCA23 and SCA24. Similar to the bromo group in SCA7, introduction of a fluoride in SCA25 retained productive conjugation with SHP1. Finally, a methyl group introduced to the ortho position of the warhead dampens conjugation (SCA26). Thus, we collectively identified SCA9, SCA7 and SCA25 as the most potent SHP1 covalent binders with Cys102. We then advanced these compounds to biochemical and functional SHP1 studies. Analogs representing the full breadth of observed SHP1 engagement are provided in the SI **(Figure 4d & Extended Data Figure 2a,b)**.

Engagement of Cys102 by SCAs relieves SHP1 auto-inhibition and elevates SHP1 phosphatase activity. In our structural model, the conformation of the SCA1-SHP1 complex suggested that Cys102 modification could facilitate rearrangements of the N-SH2 domain. To examine the SCA1 binding mode and characterize the structural effects of SCA1 binding to SHP1, we used hydrogen/deuterium exchange mass spectrometry (HDX-MS) to probe the effects of Cys102 modification on structural dynamics of SHP1. HDX-MS analysis of human SHP1 alone indicated distinct HDX profiles for the N- and C-SH2 domains with highly dynamic inter-domain linker regions and C-terminal tail **(Supplementary Table 4)**. In addition, low deuterium incorporation into the backbone was observed for majority of the PTP domain including peptides that span the active site, suggesting a stable structure, which is expected for the auto-inhibited form of the enzyme **(Supplementary Table 4)**. In order to produce uniformly labeled SHP1, we used the SCA1 analog SCA9, which labeled Cys102 to 100% stoichiometry **(Figure 4d)**. Not surprisingly, protection from deuterium incorporation was evident for SCA9 modified SHP1 in those peptide regions proximal to Cys102, due to reduced flexibility resulting from SCA9 anchorage in the binding pocket **(Figure 4e)**. This protection was either at the earliest time points for Met1-Asp8 and Phe248-Gln254 in the N-SH2 and C-SH2-PTP linker region, or at the later time points for Leu18-Gly20, Leu28-Leu41, and Ile54-Gln55 in the N-SH2 domain. Incubation with SCA9 resulted in an early deprotection of the C-SH2 domain, and increased protection of the N-SH2 domain over time **(Figure 4e & Supplementary Table 4)**. Specifically, increases in deuterium incorporation for the extreme C-terminus of the C-SH2 domain for Leu209-Asn219 was observed. These increased exchange rates were also supported by molecular dynamics simulations **(Extended Data Figure 2c & Supplementary Table 5)**.

The binding mode of SCA1, and consequent structural effects on SHP1 by SCA9, suggests that these molecules could destabilize the auto-inhibited state of SHP1 and enhance SHP1 phosphatase activity. We examined recombinant human SHP1 activity and found that SCA1 activated SHP1, exhibiting an apparent EC_{50} of 36.4 μM and maximal activity of 14.2 pmol min^{-1} **(Figure 4f)**. We examined the kinetics of activation and engagement of SHP1 by SCA1, observing time and concentration dependence **(Extended Data Figure 2d,e)**. SCA1 activation occurred in the presence of thiol reducing agents, and a SCA1 analog lacking the acrylamide warhead (SCA1-NC) largely abrogated activation **(Figure 4g)**. SCA9, SCA7 and SCA25, all of which afforded improved SHP1 engagement also further enhanced SHP1 phosphatase activity compared to SCA1 **(Figure 4d,h)**. It is worth noting the lower solubility of SCA25 and SCA7 precluded increasing concentrations beyond 40 μM and 120 μM respectively, limiting the assessment of EC_{50} across a wider concentration range. As such, the observed SAR is consistent with the predicted binding mode. Together, HDX-MS and biochemical activity data supported a model whereby SCA1 and analogs destabilized the auto-inhibited form of SHP1 at the C-SH2-PTP domain linker to lower the activation barrier to rearrangement that is necessary to access phosphorylated substrate.

SCAs engage SHP1 Cys102 and inhibit TLR4-mediated IRAK1 signaling and pro-inflammatory cytokine response in cells and *in vivo*. We next examined the cellular effects of SCAs on SHP1 regulated immunological processes. In macrophages and dendritic cells, activated SHP1 binds cytokine receptors and IRAKs to antagonize IRAK-mediated downstream NF-κB signaling[42,43]. Of note, SHP1 mediated antagonism of IRAK1 signaling is thought to be attributable in part to its phosphatase activity as well as to its binding with IRAK immunoreceptor tyrosine-based inhibitory motifs (ITIM), both of which are driven by the active conformation SHP1 upon relief of auto-inhibition[42,43]. To understand the functional consequences of SHP1 Cys102 engagement, we evaluated the signaling responsible for production of pro-inflammatory cytokines in mouse iBMDMs treated with SCA1 and SHP1 inactive SCA1-NC derivative. Following stimulation of TLR4 signaling by lipopolysaccharide (LPS), macrophage cytokine production is initiated by IRAK1 potentiation of IKK-mediated downstream degradation of phosphorylated IκBα, which leads to NF-κB phosphorylation[42]. We found near complete depletion of IκBα by 15 min following LPS stimulation, which recovered by 120 min, matching the established kinetics previously reported[47] **(Figure 5a)**. Low micromolar SCA1 prevented acute degradation of IκBα proteins, and prevented phosphorylation of the NF-κB p65 subunit upon stimulation by LPS (**Figure 5a)**. The SCA1-NC derivative lacking the warhead required to modify SHP1 Cys102 had no effect on this pathway **(Figure 5b)**.

We next examined whether optimized SCA1 derivatives effectively engaged SHP1 in cells by assessing competitive SHP1 binding with biotinylated SCA1, as described in **Figure 3**. Notably, optimized SHP1 agonists SCA9, SCA7 and SCA25 also effectively engaged SHP1 in iBMDMs, while SCA1-NC did not **(Figure 5c & Extended Data Figure 2b & 3a).** Additionally, we selected two of the improved SCAs (SCA9 and SCA5) and the SCA1-NC derivative for CPT-MS to query proteome wide engagement in iBMDMs under native conditions. Like SCA1, we found SCA9 and SCA5 also exhibited proteome wide selectivity for SHP1 Cys102 while inactive SCA1-NC showed no selectivity for SHP1 Cys102 **(Figure 5d, Extended Data Figure 3b & Supplementary Table 6)**. Interestingly, SCA9 and SCA5 did not engage the only reproducible off-target observed for SCA1, Cys153 on DHX40 **(Supplementary Table 6)**. Next, we profiled a panel of SHP1 agonists and structurally similar SHP1 inactive SCA1 derivatives for modulation of TLR4-dependent IRAK1 signaling. SCA derivatives SCA9, SCA7 and SCA25 exhibiting both improved SHP1 engagement **(Extended Data Figure 2b & Figure 5c,d)** and enhanced SHP1 phosphatase activation **(Figure 4h),** also demonstrated more robust inhibitory effects on TLR4-mediated IRAK1 signaling and downstream NF-κB activation at low micromolar concentrations **(Figure 5e)**. Conversely, structurally similar SCA1 derivatives SCA1-NC that lack the covalent warhead, or SCA6 that is a weak SHP1 labeler **(Figure 4d & Extended Data Figure 2a,b)** exhibited no effect on macrophage TLR4 signaling **(Figure 5e)**. The observed cellular structure-activity relationship is consistent with the predicted binding mode and provided a strong correlation between capacity for SHP1 Cys102 engagement and effects on TLR4-mediated IRAK1 signaling. Together, these data support that the effects of SCAs on TLR4-mediated IRAK1 signaling depended on engagement of SHP1 Cys102.

We next examined effects of SCAs on pro-inflammatory cytokine production downstream of TLR4-mediated activation of NF-κB. SCA1 inhibited production of NF-κB dependent pro-inflammatory cytokines including IL6 and TNF upon LPS stimulation **(Extended Data Figure 3c)**. For SCA1 derivatives showing improved SHP1 engagement and activation, NF-κB inhibitory effects correlated with improved IC_{50} on cytokine production **(Figure 5f)**. Moreover, in the context of TLR-dependent IL-6 and IL-1β production, SCA1 derivatives SCA5 and SCA9 inhibited IL-6 and IL-1β levels with single digit micromolar potency **(Extended Data Figure 3d,e)**. Together these findings show that SCAs mediated targeting of the Cys102 redox switch on SHP1 regulates the macrophage cytokine response to an acute pro-inflammatory stimulus. While the profile of SHP1 engagement by the SCA series correlated well with cellular efficacy on NF-κB signaling and cytokine production, it is possible that SCAs may also engage other targets relevant to the macrophage cytokine response. Nonetheless, CPT-MS of SCA1 and SCA9 indicated highly selective target engagement with SHP1 in cells and failed to identify reproducible off-targets **(Figure 2e and Extended Data Figure 3b)**.

Discussion

In this work, we developed OxImmune to systematically identify and classify hundreds of *in vivo* redox regulated cysteines on functional pockets of immune-relevant proteins. We provide a roadmap to use OxImmune to functionalize the immunological proteome by targeting redox regulated cysteine residues, as a basis for tool compound and therapeutics development. To exemplify this approach, we focused our attention on SHP1, a central inhibitor of macrophage cytokine production. Redox regulated Cys102 was found to mark a druggable pocket that modulates the auto-inhibited state of SHP1. Developing SCA1 and its derivatives to selectively target Cys102 demonstrated that engagement of this site is sufficient to relieve auto-inhibition of the protein and enhance phosphatase activity. SHP1 controls signaling from multiple immune cell surface receptors, and in macrophages we demonstrated robust regulation of TLR4-mediated activation of NF-κB. Given the broad regulatory role of SHP1, in the future, it will be interesting to examine how modulation of Cys102 affects other SHP1-dependent signaling pathways in other immune cell types, for example the JAK/STAT cytokine pathways, and Src-kinase mediated cell adhesion and integrin pathways. Specifically, it will be important to examine established TCR targets such as TCRζ, LCK, FYN, and zeta chain-associated protein of 70 kDa (ZAP70)[48,49]. More broadly, a more complete understanding of cell- and context-dependent targets of activated SHP1 will be an interesting application of the SCA series. Significant evidence supports a role for activation of SHP1 in antagonizing autoimmune disorders including rheumatoid arthritis and multiple sclerosis[38-40]. Further development of SCAs in this context could also provide new therapeutic approaches in these diseases. OxImmune analysis of SHP1

Cys102 determined that this site is subject to endogenous redox regulation *in vivo*. It is therefore likely that this site is subject to endogenous regulation by redox active metabolites, which could modulate SHP1 activity in the contexts described above. Further work examining the relevance of endogenous regulation of Cys102, or suppression of this modification, could illuminate the biological contexts where SHP1 activity is relevant in physiology or pathophysiology. More broadly, using the path taken with SHP1 as an exemplar, we expect that OxImmune will provide a foundation for therapeutic exploitation of functional pockets on proteins that regulate the immune system.

Figure Legends

Fig. 1 | Systematic discovery of redox regulated cysteines on immunological proteins.
a, Strategy to define redox regulated cysteines on immunological proteins. Immune proteins defined by InnateDB were aligned to identify cysteines conserved between mouse and human. Conserved cysteines were classified for their propensity to be oxidized *in vivo* and functionally and structurally annotated.
b, Categorization of immunological cysteines subject to dynamic oxidation (>10% difference in oxidation between any two tissues/conditions in Oximouse (data from ref. 14)).
c-f, Top 10 redox regulated cysteines on kinases **(c)**, transcription factors **(d)**, phosphatases **(e)**, and metabolic enzymes **(f)** with percent reversible oxidation across tissues/conditions with lowest and highest average oxidation in the Oximouse dataset (data from ref. 14). Data are mean ± s.e.m., n=5 for each tissue.
g, Mapping of redox regulated cysteines to experimentally determined structural and functional domains across the immunological proteome.
h, Prominent examples of high value immune targets with redox regulated cysteines on structural or functional domains, such as active and allosteric sites.

Fig. 2 | Deep chemoproteomics functionalizes the redox-sensitive Cys102 on SHP1.
a, Oximouse redox proteomics minimum (Min) and maximum (Max) percent reversible oxidation of SHP1 Cys102 across all tissues studied (n=5 for each tissue). Data are mean ± s.e.m. See Oximouse data from ref. 14.
b, Crystal structure of human SHP1 highlighting Cys102 (orange) in the closed, inactive form (left, PDB ID: 2B3O), residing within an N-SH2 proximal pocket involved in rearrangement to the open, active form (right, PDB ID: 3PS5). N-SH2: N-terminal SH2 domain (green); C-SH2: C-terminal SH2 domain (brown); PTP: protein tyrosine phosphatase domain (grey). Disordered regions are shown in blue; active site pocket is represented in red.
c, Schematic of CPT-MS workflow for quantification of cysteine sites engagement with 53 cysteine-reactive small molecules, illustrating CPT labeling, TMT multiplexing, IMAC enrichment, fractionation, and MS analysis.
d, Stoichiometric engagement score (R) of each cysteine quantified in human THP-1 MDM cysteine proteome treated with SCA1 (20 μM), showing SHP1 Cys102 as a top hit exhibiting >50% engagement by SCA1. R = (S/N of DMSO) / (S/N of SCA1), where S/N is signal-to-noise ratio.
e, Pairwise comparisons of R for each cysteine quantified in human THP-1 MDM replicates treated with 5, 10, 20, or 40 μM SCA1 for 3 h (37°C), followed by CPT enrichment.
f, SHP1 Cys102 site-specific percent modification by SCA1 in THP-1 MDMs at the indicated concentrations. Data are mean ± s.d. of n=2 biological replicates.
g,**h**, SHP1 **(g)** or SHP2 **(h)** cysteines site-specific percent modification by SCA1 in THP-1 MDMs at the indicated concentrations. Data are mean ± s.d. of n=2 biological replicates.

Fig. 3 | SCA1 selectively engages Cys102 on SHP1.
a,c, Intact protein MS of human recombinant wild type (WT) or Cys102 to Ser102 mutant (C102S) SHP1 (2 μM) incubated with DMSO, 5 or 10 molar equivalents of SCA1 for 24 h (4°C).
b, Quantitative MS determination of the proportion of free cysteine in human recombinant SHP1 incubated with DMSO or 10 molar equivalents of SCA1 for 2 h (room temperature) (n=3). Data are mean ± s.e.m. ****P=0.000104 (multiple unpaired t-tests).

d, SHP1 binding by biotinylated SCA1 in iBMDM or THP-1 MDM lysates treated overnight (4°C) at the indicated concentrations and enriched by streptavidin pulldown. Immunoblots shown are representative of three independent experiments.
e, SHP1 binding by SCA1 in iBMDM or THP-1 MDM cells treated at the indicated concentrations for 3 h (37°C) followed by competition for SHP1 binding with biotinylated SCA1 (10 μM). Densitometry analyses of SHP1 immunoblots from *n*=3 independent iBMDM and *n*=2 independent THP-1 MDM experiments are shown.

Fig. 4 | Structural consequence for SHP1 Cys102 modification by SCA1 and analogs.
a, Covalent docking and molecular dynamics simulations of SCA1 to active conformation SHP1 (PDB ID: 3PS5). Surface representation of SCA1 (gray, sticks) and Cys102 (yellow) binding pocket consisting of residues on both SH2 domains including Arg3 to Arg7, Pro31 to Phe39 and the loop between them (brown). The binding mode of SCA1 is stabilized by cation-π interactions between SCA1 phenyl ring and Arg7 (green, sticks), edge-to-π interaction between pyrazolopyrimidine and Phe39 (green, sticks), and hydrogen bonds between acrylamide amine and Phe5 (red, dashes). The binding mode also showed space rigidity between Cl atom and His114, Leu139, and Met1 (green, sticks) and solvent exposure of phenyl ring meta position.
b,c, Chemical optimization of SCA1 and corresponding SHP1 target engagement measured by intact protein MS of human recombinant SHP1 (2 μM) incubated with the indicated SCA1 analogs at 10 molar equivalents (20 μM) for 24 h (4°C). Percent SHP1 engagement represents relative abundance of small molecule engaged SHP1 to relative abundance of unlabeled SHP1.
d, Percent SHP1 engagement of human recombinant SHP1 (2 μM) incubated with the full breadth of SCA1 analogs at 10 molar equivalents (20 μM) for 24 h (4°C) and measured by intact protein MS. Percent SHP1 engagement represents relative abundance of small molecule engaged SHP1 to relative abundance of unlabeled SHP1. Data are mean ± s.d. of two independent experiments.
e, Deuterium uptake difference plot between SHP1 (10 μM) incubated with SCA9 (100 μM) and SHP1 alone for a subset of SHP1 peptides (top panel) and represented on SHP1 open, active crystal structure (PDB ID: 3PS5) (bottom panel). Red ribbon indicates the SHP1 active site pocket. Full list of identified SHP1 peptides is provided in **Supplementary Table 4**.
f, Recombinant human SHP1 phosphatase enzymatic activity following 2 h pre-incubation (room temperature) with DMSO or SCA1 at the indicated concentrations. Phosphatase activity as a function of SCA1 concentration relative to DMSO control measured at 37°C is shown.
g, Recombinant human SHP1 phosphatase enzymatic activity following 2 h pre-incubation (room temperature) with DMSO or non-covalent reversible analog of SCA1 (SCA1-NC) at the indicated concentrations. Phosphatase activity as a function of SCA1-NC concentration relative to DMSO control measured at 37°C is shown.
h, Recombinant human SHP1 phosphatase enzymatic activity following 2 h pre-incubation (room temperature) with DMSO, SCA7, SCA9 or SCA25 at the indicated concentrations. Phosphatase activity as a function of SCA analog concentration relative to DMSO control measured at 37°C is shown.
All data are mean ± s.e.m., *n*=4, unless otherwise specified.

Fig. 5 | Covalent SHP1 agonists antagonize TLR4 signaling and pro-inflammatory cytokine response in macrophages and *in vivo*.
a, LPS-induced (100 ng/ml) IκBα degradation and NF-κB p65 phosphorylation over a time course of 2 h in iBMDMs pre-treated with DMSO or SCA1 (50 μM) for 3 h. Immunoblots shown are representative of three independent experiments.
b, LPS-induced (100 ng/ml) IκBα degradation and NF-κB p65 phosphorylation in iBMDMs following 3 h pre-incubation with DMSO, SCA1 or its non-covalent reversible analog of SCA1 (SCA1-NC) at the indicated concentrations. Immunoblots shown are representative of three independent experiments.
c, SHP1 binding by SCA derivatives in iBMDMs treated at 5 μM followed by competition for SHP1 binding with biotinylated SCA1 (10 μM).

d, Stoichiometric engagement score (R) of each cysteine quantified in iBMDM cysteine proteome treated with SCA9 (50 μM), showing SHP1 Cys102 as top hit exhibiting >50% engagement by SCA9. R = (S/N of DMSO) / (S/N of SCA9), where S/N is signal-to-noise ratio.
e, LPS-induced (100 ng/ml) IκBα degradation and NF-κB p65 phosphorylation in iBMDMs following 3 h pre-incubation with DMSO or SCA derivatives at the indicated concentrations. Immunoblots shown are representative of two independent experiments.
f, Pro-inflammatory cytokine IL-6 and TNF levels in cell supernatants of iBMDMs pre-incubated 3 h with SCA1, SCA1-NC or the respective derivatives over a dose response (0.313-80 μM) followed by 6 h LPS stimulation (100 ng/ml). Normalized percent cytokine production as a function of concentration are used to calculate IC_{50} values.

Extended Data Fig. 1 | Selectivity of SCA1 engagement with SHP1 Cys102 across iBMDM cysteine proteome.
a, Pairwise comparisons of R for each cysteine quantified in iBMDM replicates treated with 5, 10, 20, or 40 μM SCA1 for 3 h (37°C), followed by CPT enrichment. R = (S/N of DMSO) / (S/N of SCA1), where S/N is signal-to-noise ratio.
b, SHP1 Cys102 site-specific percent modification by SCA1 in iBMDMs at the indicated concentrations. Data are mean ± s.d. of *n*=2 biological replicates.
c,**d**, SHP1 **(c)** or SHP2 **(d)** cysteines site-specific percent modification by SCA1 in iBMDMs at the indicated concentrations. Data are mean ± s.d. of *n*=2 biological replicates.

Extended Data Fig. 2 | Characterization of SHP1 binding and phosphatase activation kinetics by SCA1 and analogs.
a, Percent SHP1 engagement of human recombinant SHP1 (2 μM) incubated with the full breadth of SCA1 analogs at 5 molar equivalents (10 μM) for 24 h (4°C) and measured by intact protein MS. Percent SHP1 engagement represents relative abundance of small molecule engaged SHP1 to relative abundance of unlabeled SHP1. Data are mean ± s.d. of two independent experiments.
b, Full list of structures of SCA1 analogs at the indicated molar equivalents and their respective percent SHP1 engagement as measured by intact SHP1 protein (2 μM) MS are shown.
c, Differential backbone amine proton solvent accessible surface area (BB NH proton differential SASA) between SCA9 bound and apo SHP1 calculated from molecular dynamics simulations. Highlighted peptide regions that showed extensive uptake of deuterium were also more solvent exposed upon SCA9 binding during molecular simulations. For full list of molecular simulations peptides, refer to **Supplementary Table 5**.
d, Recombinant human SHP1 phosphatase enzymatic activity following 30 min pre-incubation (room temperature) with DMSO or SCA1 (10 μM) measured at 37°C and represented as phosphate equivalents released over a time course of 2 h. Data are mean ± s.e.m., *n*=4.
e, Intact protein MS of human recombinant SHP1 (2 μM) incubated with 10, 15, 20, 25, 30, 35, 40, 45, or 50 molar equivalents of SCA1 for 48 h (4°C). Percent SHP1 labeling represents relative abundance of SCA1 engaged SHP1 to relative abundance of unlabeled SHP1.

Extended Data Fig. 3 | SCAs effects on macrophage pro-inflammatory cytokine response and *in vivo*.
a, SHP1 binding by SCA1 derivatives in iBMDMs treated at 20 μM followed by competition for SHP1 binding with biotinylated SCA1 (10 μM).
b, Pairwise comparisons of R for each cysteine quantified in iBMDM replicates treated with 50 μM SCA9, SCA5 or SCA1-NC for 3 h (37°C), followed by CPT enrichment. R = (S/N of DMSO) / (S/N of SCA), where S/N is signal-to-noise ratio.
c-e, Pro-inflammatory cytokine IL-6 and TNF levels in cell supernatants of iBMDM pre-incubated 3 h with SCA1, SCA1-NC or the respective derivatives over a dose response (0.313-80 μM) followed by 6 h LPS stimulation (100 ng/ml). For measurement of pro-inflammatory cytokine IL-1β levels in cell supernatants, iBMDMs were pre-treated with LPS (100 ng/ml) for 3 h followed by treatment with DMSO or SCA9 at the indicated

concentrations for 45 min and primed with adenosine triphosphate (ATP, 5 mM) for 45 min. Normalized percent cytokine production as a function of concentration are used to calculate IC_{50} values. Data are mean ± s.e.m., n=4.

Methods

Generation of the innate immune cysteine dataset

The innate immune cysteine dataset was generated using R (Version 4.2.1). The innate immune gene dataset was obtained from the InnateDB website[17] (downloaded February 2023: https://www.innatedb.com/). The human proteome (Uniprot: downloaded February 2023: https://www.uniprot.org) was filtered for gene names found in InnateDB to establish a dataset of human innate immune proteins. To match conserved mouse cysteine residues to the corresponding human cysteines, mouse and human protein sequences were obtained from Uniprot (downloaded February 2023: https://www.uniprot.org). Sequence datasets were matched by Uniprot names and sequences of matched proteins were aligned using the msa package in R and the ClustalOmega sequence alignment function[50]. Cysteine positions of conserved cysteines in mouse were extracted and matched to corresponding cysteines in human. To determine the redox regulatory potential of cysteines, reversible cysteine oxidation data was retrieved from the Oximouse dataset[14] (https://oximouse.hms.harvard.edu). The average cysteine oxidation for each tissue and age group within the oximouse was calculated and the delta percent oxidation between the maximum and minimum average oxidation was determined for each cysteine. Cysteine oxidation values were then matched to mouse cysteines that are conserved in human and the dataset was filtered for cysteines within innate immune proteins. Pfam domain annotations (downloaded from https://www.ebi.ac.uk/interpro/: Human February 2024, Mouse April 2023) were matched to all human cysteines and all conserved mouse cysteines. Identifiers of available protein structure (AlphaFold and PDB, obtained from Uniprot: downloaded February 2023: https://www.uniprot.org) for each species were mapped to the cysteines. Cysteines were further annotated by mapping the following database annotations to the generated innate immune cysteine dataset: Phosphatases (downloaded February 2023 from the DEPOD website[51]: https://depod.bioss.uni-freiburg.de), kinases (downloaded February 2023 from the KinaseMD website[52]: https://bioinfo.uth.edu/kmd/index.html), Human Protein Atlas (Protein Class information downloaded February 2023 from the Human Protein Atlas website[53]: https://www.proteinatlas.org), transcription factors (downloaded February 2024 from the TFLink website[54]: https://tflink.net), and metabolic enzymes (downloaded February 2024 from the Mammalian Metabolic Enzymes Database website[55]: https://esbl.nhlbi.nih.gov/Databases/KSBP2/Targets/Lists/MetabolicEnzymes/MetabolicEnzymeDatabase.html) .

OxImmune web application

The OxImmune web application (https://chouchani-lab.shinyapps.io/oximmune/) was developed using the Shiny R package (v1.8.0; https://shiny.posit.co/). Data visualizations were constructed with the following packages in R: 'DT': (https://rstudio.github.io/DT/), 'shinyjs': (https://github.com/daattali/shinyjs), 'shinydashboard': (https://rstudio.github.io/shinydashboard/), 'glue': (https://glue.tidyverse.org/), 'png': (https://www.rforge.net/png/), 'readxl': (https://readxl.tidyverse.org/), 'readr': (https://readr.tidyverse.org/), and 'plotly': (https://plotly-r.com/). 3D protein structural models were accessed from the AlphaFold Database (https://alphafold.ebi.ac.uk/) using the 'shiny.molstar' package. The OxImmune web application is based on the innate immune cysteine dataset generated above.

Cell culture

Immortalized bone marrow-derived macrophages (iBMDMs) (prepared from WT C57BL/6 mice, a gift from Prof. J. Kagan (Boston Children's Hospital, Boston, MA, USA)[56]) were cultured in Dulbecco's modified eagle medium (DMEM), high glucose, GlutaMAX supplement (Gibco, #10566016) supplemented with 10% (vol/vol) heat-inactivated fetal bovine serum (Hyclone), 100 U/ml penicillin and 100 µg/ml streptomycin (Gibco, #15140122), 1 mM sodium pyruvate, in a humidified 37°C, 5% CO_2 tissue culture incubator. THP-1 monocytes (ATCC #TIB-202) were cultured in RPMI 1640, GlutaMAX supplement, HEPES (Gibco, #72400047) supplemented with 10% (vol/vol) heat-inactivated fetal bovine serum (Hyclone), 100 U/ml penicillin and 100 µg/ml streptomycin (Gibco, #15140122), in a humidified 37°C, 5% CO_2 tissue culture incubator. THP-1

monocytes were differentiated into macrophages with 10 ng/ml phorbol 12-myristate 13-acetate (PMA) for 24 h (Sigma Aldrich, #P1585).

Cysteine-reactive phosphate tag mass spectrometry (CPT-MS)

For cysteine-reactive small molecules screen in iBMDMs and THP-1 MDMs, cells were plated in 10-cm dishes and allowed to adhere overnight. Cells were then lysed in 500 µl/dish PBS, tip-sonicated (QSonica Q500 Sonicator, 10 pulses, 30% amplitude for 10sec per pulse, 5 sec pause between pulses), and protein concentration quantified by bicinchoninic acid (BCA) assay (Pierce BCA protein assay kit, #23225). Lysates were split into 8 300 µg protein aliquots, and treated with 5, 10, 20 or 40 µM SCA1 or DMSO in duplicates, or 50 µM SCA9, SCA5 or SCA1-NC in replicates, for 3 h at 37°C on a shaking incubator. Samples were then subjected to methanol-chloroform precipitation and the pellets were washed twice with methanol. Following precipitation, protein pellets were re-dissolved in cysteine-reactive phosphate tag (CPT) (in-house) labelling buffer (50 mM HEPES, pH 8.5, 2% SDS, 10 mM CPT, 5 mM TCEP) and incubated for 2 h at 37°C on a shaking incubator in the dark. Proteins were then subjected to repeated methanol-chloroform precipitation to remove CPT and the pellets were washed twice with methanol. The resultant protein pellets were reconstituted with 100 µl 200 mM EPPS buffer, pH 8 (Sigma Aldrich, #E9502), and digested with Lys-C (Wako Chemicals, #125-05061) and trypsin (Promega, #V5113) at 100:1 substrate:enzyme ratio overnight (19 h) at 37°C.

Overnight digested samples were clarified by centrifugation at 16,000 g for 10 min, and subjected to protein concentration quantification by microBCA assay (Thermo Scientific Micro BCA protein assay kit, #23235). 250 µg peptides for each sample were labelled with tandem mass tag (TMT)pro-18plex reagents (Thermo Scientific, #A44520) in 30% acetonitrile (ACN)/EPPS solution for 1 h at room temperature. TMT labelling was then quenched with 5% hydroxylamine for 15 min and samples were acidified with 1% formic acid (FA) (pH<3). A ratio check was performed by mixing 1% (vol/vol) sample from each TMT channel, and standardized TMT-labelled peptides were evenly pooled according to the ratio check. Pooled sample was then desalted by Sep-Pak C18 cartridge (Waters, #WAT054945, 200 mg). Briefly, cartridge was equilibrated with 6 ml 100% ACN, 2 ml 70% ACN/1% FA, 6 ml 1% FA, loaded with sample, washed with 6 ml 1% FA, and eluted with 0.6 ml 40% ACN/1% FA followed by 1.2 ml 70% ACN/1% FA, all steps allowed for gravity flow. Elution sample was frozen and lyophilized by speed vac. Following which, phosphate groups on endogenously phosphorylated peptides were removed through Lambda phosphatase treatment by redissolving the peptides in 500 µl phosphatase treatment buffer (50 mM HEPES, pH 7.5, 100 mM NaCl, 1 mM $MnCl_2$, 12 µl Lambda phosphatase (Santa Cruz Biotechnology, #sc-200312)), and incubated for 2 h at 30°C on a shaking incubator. Phosphatase-treated samples were acidified with 10% trifluoroacetic acid (TFA) (pH<3) desalted once more by Sep-Pak C18 cartridge (Waters, #WAT054955, 50 mg). Briefly, cartridge was equilibrated with 0.9 ml 100% ACN, 0.3 ml 70% ACN/1% FA, 0.9 ml 0.1% TFA, loaded with sample, washed with 0.9 ml 0.1% TFA, and eluted with 0.3 ml 40% ACN/1% FA followed by 0.35 ml 70% ACN/1% FA, all steps allowed for gravity flow. Elution sample was frozen and lyophilized by speed vac.

CPT-labeled peptides were then purified by immobilized metal affinity chromatography (IMAC) using High-Select Fe-NTA Phosphopeptide Enrichment Kit (Thermo Scientific, #A32992) following manufacturer's protocol. Briefly, IMAC column storage buffer was removed by centrifugation at 1000 g for 30 sec, equilibrated with 200 µl Binding/Wash Buffer (provided in kit), centrifuged at 1000 g for 30 sec, this equilibration step repeated once, and column incubated with CPT-labelled peptides resuspended in 300 µl Binding/Wash Buffer for 30 min at room temperature on a shaking incubator. Column was centrifuged at 1000 g for 30 sec, sample washed with 200 µl Binding/Wash Buffer thrice followed by 100 µl LC-MS (liquid chromatography-mass spectrometry) grade water, and eluted with 150 µl 50 mM HK_2PO_4 (dibasic potassium phosphate, pH 10) twice by incubation for 1 min prior to centrifugation at 1000 g for 30 sec. Purified peptides were acidified with 10% TFA (pH<3) and desalted by Sep-Pak C18 50 mg cartridge as described above, and lyophilized by speed vac.

Peptides were fractionated with Agilent 1100 quaternary HPLC system. Peptides were separated with 57 min linear gradients from 3-32% ACN in 10 mM ammonium bicarbonate, pH 8, at 0.6 ml/min flow rate, into 96 fractions, which were then combined into 24 fractions. Fractionated and combined samples were lyophilized by

speed vac and desalted using StageTip, and reconstituted in 5% FA/5% ACN for liquid chromatography tandem mass spectrometry (LC-MS/MS) analysis. Protein abundances in 2 µg peptides from each fraction were measured using Orbitrap Eclipse instrument coupled to Easy-nLC 1200 (Thermo Scientific, #LC140) ultrahigh-pressure liquid chromatography (HPLC) pump and analyzed using 180 min gradients comprising 2-23% ACN, 0.125% FA, at a flow rate of 500 nl/min. A high-Frequency Asymmetric-waveform ion mobility mass spectrometry (FAIMS)Pro (Thermo Scientific, #FMS02-10001) device was used for precursors separation and operated under default settings and compensation voltages 40V/-60V/-80V. At each voltage, peptide ions were collected in data dependent mode with a mass range of m/z 400-1600 and 2 sec cycles. MS1 resolution was set to 120,000 with standard automatic gain control target. The top 20 most abundant multiply-charged ions were then selected and subjected to fragmentation at a normalized collisional energy of 35% for MS2 with a dynamic exclusion of 120 sec. MultiNotch synchronous precursor selection (SPS)-MS3 was used for isolating MS3 precursors and MS3-based TMT quantification. Ten notches were selected and the MS3 spectra were obtained in the Orbitrap using higher-energy-collisional dissociation and normalized collisional energy of 65% as previously described[14].

MS/MS spectra were searched using the Comet algorithm[57] against a database of Mus musculus protein sequences from UniProt (http://www.uniprot.org, 2020) or homo sapiens protein sequences from UniProt (http://www.uniprot.org, 2020). Reversed peptide sequences were used as decoys for false discovery rate (FDR) filtering, and common protein contaminants including human keratins and trypsin were included. Peptides search was performed following these parameters: 25 ppm precursor mass tolerance, 1.0 Da product ion mass tolerance, full tryptic digestion, ≤3 missed cleavages, variable modifications of oxidation on methionines (+15.9949), and CPT on cysteines (+221.08169), static modifications of TMT (+304.2071) on peptide N-termini and lysines[14]. To control for FDR, the target-decoy method was used. Linear discriminant analysis was employed for peptide-level FDR control at <0.5% to discriminate incorrect from correct peptide identifications. Peptides with <6 amino acids were excluded. Protein-level FDR was controlled at 1%, which further decreases peptide reverse hits. Peptides were matched to the least number of sites. TMT reporter ion signal-to-noise ratios for all peptides that were matched to the same site were used for site quantification. For SCA9, SCA5 and SCA1-NC CPT-MS experiment, sites were filtered for R with coefficient of variation <0.3 across replicates.

SHP1 protein expression and purification

C-terminal 6x His-tag constructs of human wild type (WT) or C102S full-length (residues 1-595) and residues 1-524 SHP1 were expressed using pET 21b(+) vector in Rosetta 2 and purified via affinity and size-exclusion chromatography. Briefly, transformed cells were cultured at 37°C in Terrific Broth (TB) medium for 6h, and auto-induced at 20°C for 18 h. Cell pellets were lysed by high pressure microfluidizer in lysis buffer containing 50 mM HEPES, 500 mM NaCl, 1 mM TCEP, 20 mM imidazole, pH 7.5, 0.1% IGEPAL, 10% glycerol, 1 mM phenylmethylsulfonyl fluoride (PMSF). Following lysis, the supernatant was applied to Ni-NTA for affinity binding at 4°C for 1 h with rocking, and the resin was washed by fast protein liquid chromatography (FPLC) with wash buffer containing 25 mM HEPES, 1.5 M NaCl, 1 mM TCEP, 20 mM imidazole, pH 7.5, and eluted with elution buffer containing 25 mM HEPES, 500 mM NaCl, 1 mM TCEP, 400 mM imidazole, 10% glycerol, pH 7.5. The final protein was purified by size exclusion using a HiLoad 16/600 Superdex 200 pg column (Cytiva) in buffer containing 20 mM HEPES, 200 mM NaCl, 1 mM TCEP, pH 7.5. The resultant SHP1 containing fractions were concentrated to 10 mg/ml and stored at -80°C.

Intact protein mass spectrometry

WT or C102S SHP1 recombinant protein (final concentration 2 µM) was incubated with 5 equivalents (10 µM) or 10 equivalents (20 µM) of the indicated SHP-1 agonists at 4°C for 24 h in reaction buffer (25 mM HEPES, pH 7.4, 50 mM NaCl, 2.5 mM EDTA, 100 µM TCEP). The samples were then diluted 1 in 2 with Buffer A (0.1% formic acid, 5% acetonitrile, 95% H_20), and 3.5 µg per sample was subjected to LC-MS analysis using a PLRP-S 100A, 2.1 x 50 mM, 5 µM column (Agilent) on a Q-Exactive HF-X. Separation buffers A (0.1% formic acid, 5% acetonitrile, 95% H_20) and B (0.1% formic acid in 95% acetonitrile, 5% H_20) were used for the runs at 60°C, 0.3 ml min^{-1}. The gradient used was 15% Buffer B, 0.5 min, ramped up to 95% over 4.5 min. Positive ion modes were collected with full scan analysis over 900 – 2600 *m/z* at 7500 resolution, 1 x 10^5 AGC, 25 ms maximum ion

accumulation time and 60 eV in-source collision-induced dissociation. Data processing was performed using BioPharma Finder software version 4.1 (Thermo Fisher Scientific).

Recombinant SHP1 cysteine site engagement

Recombinant SHP1 at 8.6 μM was incubated with 86 μM SCA1 or DMSO (in 10 mM HEPES, pH 7.4, 50 mM NaCl, 2.5 mM EDTA, 100 μM TCEP) for 2 h at room temperature. Following incubation, the protein was subjected to methanol-chloroform precipitation, and the resultant protein pellets were washed twice with methanol. The pellets were then resuspended in a buffer containing 2% SDS, 50 mM HEPES pH 8.5, 40 mM iodoacetamide and 5 mM TCEP, and incubated for 1 h at 37°C in the dark. The samples were then subjected to methanol-chloroform precipitation and the pellets were washed twice with methanol. The resultant protein pellets were reconstituted with 50 μl 200 mM EPPS buffer, pH 8, and digested with Lys-C and trypsin at 100:1 substrate:enzyme ratio overnight (19 h) at 37°C. Overnight digested samples were clarified by centrifugation at 16,000 g for 10 min, and subjected to protein concentration quantification by microBCA assay (Thermo Scientific Micro BCA protein assay kit, #23235). 13.8 μg peptides for each sample were labeled with TMTpro-18plex reagents (Thermo Scientific, #A44520) in 30% ACN/EPPS solution for 1 h at room temperature. TMT labelling was then quenched with 5% hydroxylamine for 15 min and samples were acidified with 20% FA (pH<3). 2 μl of each sample was pooled, diluted to 5% ACN using 1% FA, desalted by StageTip and lyophilized by speed vac. The sample was reconstituted in 5% FA/5% ACN and analyzed by LC-MS.

Biotin enrichment assay

For SCA1 competitive biotin enrichment, iBMDMs or THP-1 MDMs seeded in 10-cm dishes were pre-treated with 1.25, 2.5, 5, 10, 20 or 40 μM SCA1 or DMSO for 3 h (37°C). Following pre-treatment, cells were washed twice with ice-cold phosphate-buffered saline (PBS), lysed with 1 ml/dish lysis buffer (50 mM Tris pH 8.0, 150 mM NaCl, 1% NP-40, 5 mM EDTA, Roche EDTA-free protease inhibitor cocktail (Roche, #11836170001)), and incubated 30 min on ice. Clarified lysates (centrifugation at 16,000 g, 10 min, 4°C) were incubated with 10 μM biotinylated SCA1 overnight (16-18 h), 4°C, with rotation. For non-competitive biotin enrichment, iBMDMs or THP-1 MDMs seeded in 10-cm dishes were lysed and clarified as above, and incubated with 0.1, 1 or 10 μM biotinylated SCA1 overnight (16-18 h), 4°C, with rotation. 30 μl slurry streptavidin beads (Pierce high capacity streptavidin agarose, #20357) were added the next day, incubated for 3 h, 4°C, with rotation. Samples were washed 7 times, each with 1 ml lysis buffer indicated above. Beads were pelleted, reduced with 2X LDS (4X NuPAGE LDS sample buffer (Invitrogen, #NP0007) diluted 1 in 2) containing 5% β-mercaptoethanol, boiled at 95°C for 10 min, and subjected to western blotting analysis with anti-SHP1 (Cell Signaling, #3759, rabbit mAb; 1:1000 dilution) and anti-β-actin (Cell Signaling, #3700, mouse mAb; 1:5000 dilution) antibodies. 1% volume of pre-purified overnight biotinylated samples were included as input. Input samples were reduced and denatured as indicated above for biotin enriched samples.

Molecular modeling

Covalent docking of SCA1 was performed using CovDock in Schrödinger suite (release 2023-4) using default parameters. Cys102 was defined as the reactive residue in all covalent docking calculations. Molecular dynamics (MD) simulations were performed with Desmond in Schrödinger suite with OPLS-4 forcefield and NPT ensemble. A selected binding mode after visual inspection was used as initial structure for MD simulations. Orthorhombic simulation box with buffer of 12 Å and TIP3P water model were applied. Default equilibration protocol was used, and simulations were carried out at 293 K at 1 atm pressure. Production run was 1 μs, and the last 500 ns trajectory was used to analyze the interactions and identify the most populated configurations through trajectory clustering. Solvent accessible surface areas of selected atoms (i.e. backbone amine proton) were calculated using customized python scripts with Schrödinger suite API.

Hydrogen/deuterium exchange mass spectrometry

Complete HDX-MS methods are included in **Supplementary Table 4**. In brief, prior to HDX-MS analyses, SHP1 recombinant protein (10 μM) was incubated with 10 equivalents (100 μM) of SCA9 at 4°C for 24 h in reaction buffer (25 mM HEPES, pH 7.4, 50 mM NaCl, 2.5 mM EDTA, 100 μM TCEP). Deuterium labeling was initiated

with an 18-fold dilution into D_2O labeling buffer (36 µl, 10 mM HEPES-KOH, 50 mM NaCl, 100 µM TCEP, 2.5 mM EDTA, pD 7.4, 99.9% D_2O). The labeling reaction was quenched at time points 10 seconds, 30 seconds, 1 minute, 3 minutes, 10 minutes, 1 hour, and 4 hours with the addition of an equal volume of ice-cold quenching buffer (150 mM potassium phosphate pH 2.4, H_2O) and immediately injected into a Waters HDX system. Deuterated and control samples were digested online at 15°C using a AffiPro Nep-2 column (AffiPro, AP-PC-004) and peptides were trapped and desalted on a VanGuard Pre-Column trap [2.1 mm × 5 mm, ACQUITY UPLC BEH C18, 1.7 µm (Waters, #186002346)] for 3 minutes at 100 µl/min. Peptides were eluted from the trap using a 5%-35% gradient of acetonitrile with 0.1% formic acid over 6 minutes at a flow rate of 100 µl/min, and separated using an ACQUITY UPLC HSS T3, 1.8 µm, 1.0 mm × 50 mm column. Mass spectra were acquired using a Waters Synapt G2-Si HDMS^E mass spectrometer in ion mobility mode. Peptides were identified from replicate analyses of undeuterated control samples using PLGS 3.0.1 and relative amounts of deuterium incorporated into each peptide were determined using DynamX 3.0. The deuterium uptake values used to generate all difference maps presented in **Figure 4e** are provided in **Supplementary Table 4**. Deuterium levels were not corrected for back exchange and thus reported as relative[58]. All HDX-MS data have been deposited to the ProteomeXchange Consortium via the PRIDE (PMID: 34723319) partner repository with dataset identifier PXD055006. Note for reviewers' access to data: Username: reviewer_pxd055006@ebi.ac.uk, Password: xO7zu05dQFvz

SHP1 phosphatase activity assay

SHP1 phosphatase activity was assessed by monitoring dephosphorylation of the synthetic substrate DiFMUP (6,8-Difluoro-4-Methylumbelliferyl Phosphate) (Thermo Fisher Scientific, #D6567) to the fluorogenic product DiFMU (6,8-Difluoro-7-Hydroxy-4-Methylcoumarin) (Thermo Fisher Scientific, #D6566). Briefly, 100 nM recombinant SHP1 was incubated with SCA1, SCA1-NC, SCA7, SCA9, or SCA25 at the indicated concentrations for 2 h at room temperature in activity buffer (25 mM HEPES, pH 7.4, 50 mM NaCl, 2.5 mM EDTA, 100 µM TCEP). Following incubation, the reaction was initiated by addition of 80 µl pre-incubated enzyme to 20 µl DiFMUP substrate (final concentration 50 µM) in a 96-well plate (Corning, #3603) at 37°C. Fluorescence at excitation/emission wavelengths of 355/460 nm was continuously measured in a fluorescence-based SpectraMax M5 microplate reader (Molecular Devices), and converted to phosphate equivalents released using a DiFMU reference standard curve. The turnover to one picomole of DiFMU is equivalent to release of one picomole of phosphate. Rate of SHP1 activity in the presence of each agonist was calculated as picomole phosphate release per min in fold change relative to DMSO control, and the rates fitted on a non-linear regression model on GraphPad Prism 9, with calculated EC_{50} and V_{max} of the reactions as indicated.

Cellular NF-κB activation assay

iBMDMs seeded in 24-well plates at $2x10^6$/ml were allowed to adhere overnight. The following day, cells were pre-treated with the indicated concentrations of compounds for 3 h, followed by lipopolysaccharide (LPS) (InvivoGen, LPS-EK Ultrapure, #tlrl-peklps) induction at 100 ng/ml for 15 min. Cells were washed with ice-cold phosphate-buffered saline (PBS) and lysed in 80 µl/well of Triton-lysis buffer (25 mM Tris-HCl, pH 7.5, 100 mM NaCl, 2.5 mM EDTA, 2.5 mM EGTA, 20 mM NaF, 1 mM Na3VO4, 20 mM sodium β-glycerophosphate, 10 mM sodium pyrophosphate, 0.5% Triton X-100, Roche EDTA-free protease inhibitor cocktail (Roche, #11836170001) and 0.1% β-mercaptoethanol). Lysates were pre-cleared by centrifugation at 21,000 g, 10 min, 4°C, reduced with 4x NuPAGE LDS sample buffer (Invitrogen, #NP0007) containing 5% β-mercaptoethanol, and boiled at 95°C for 10 min. Equal amounts of proteins were resolved using NuPAGE 4-12% Bis-Tris 15-well or 26-well gels (Invitrogen, #NP0336BOX or #WG1403BOX), transferred onto PVDF membranes (Thermo Fisher Scientific, iBlot 2 Gel Transfer Device, #IB21001), and immunoblotted with anti-IRAK1 (Cell Signaling, #4504, rabbit mAb; 1:1000 dilution), anti-phospho-IκBα (Ser32/36) (Cell Signaling, #9246; mouse mAb; 1:1000 dilution), anti-IκBα (Cell Signaling, #9242, rabbit pAb; 1:1000 dilution), anti-phospho-NFκB p65 (Ser536) (Cell Signaling, #3033, rabbit mAb; 1:1000 dilution), anti-NFκB p65 (Cell Signaling, #8242, rabbit mAb; 1:1000 dilution), and anti-β-actin (Cell Signaling, #3700, mouse mAb; 1:3000 dilution) antibodies, diluted in TBS-T (Boston BioProducts, Inc., #IBB-180X) containing 5% BSA, followed by incubation with horseradish peroxidase-conjugated anti-rabbit or anti-mouse secondary antibodies (Promega, #W4011 or #W4021), diluted

1:10000 in TBS-T containing 5% milk, and visualized using ECL western blotting substrates (Pierce ECL Western Blotting Substrate, #32106).

Cytokine production quantification via ELISA assays

iBMDMs seeded in 96-well plates at $2x10^6$/ml were allowed to adhere overnight. The following day, cells were pre-treated with the indicated concentrations of SCA1 or derivatives for 3 h, followed by LPS induction at 100 ng/ml for 6 h. IL-6 and TNF cytokine levels in cell culture supernatants were quantified using mouse IL-6 or TNF DuoSet ELISA kits (R&D Systems, #DY406 or #DY410) according to manufacturer's protocols. For measurement of pro-inflammatory cytokine IL-1β levels in cell supernatants, iBMDMs seeded and allowed to adhere as above are pre-treated with LPS (100 ng/ml) for 3 h followed by treatment with DMSO or SCA9 at the indicated concentrations for 45 min and primed with adenosine triphosphate (ATP, 5 mM) for 45 min. IL-1β levels in cell supernatants were quantified using mouse IL-1β DuoSet ELISA kit (R&D Systems, #DY401) according to manufacturer's protocols. Absorbance values at 450 and 540 nm were determined with a microplate reader (BMG LABTECH FLUOstar Omega microplate reader), and wavelength corrected absorbances were used to plot standard curves from which cytokine levels from supernatant samples were calculated by intrapolation using a 4-parameter logistic (4PL) regression on GraphPad Prism 9.

Figures and illustrations

Figures were prepared in Adobe Illustrator 2024, GraphPad Prism 9, PyMOL (Version 2.3.1), ChemDraw (Version 22.2.0), R (Version 4.2.1), and illustrations in BioRender (https://www.biorender.com/) with publication licenses. Protein structures (indicated PDB IDs) were obtained from the PDB website (https://www.rcsb.org).

Data Availability

Mass spectrometry proteomics data will be deposited to the ProteomeXchange Consortium via the PRIDE partner repository and made public accessible upon acceptance. HDX mass spectrometry proteomics data have been deposited to the ProteomeXchange Consortium via the PRIDE partner repository with the dataset identifier PXD055006. All data associated with this work are otherwise provided in the manuscript, and will be provided upon request to the corresponding author.

Acknowledgements

This work was supported by the Claudia Adams Barr Program (E.T.C.), the Lavine Family Fund (E.T.C.), the Pew Charitable Trust (E.T.C.), NIH DK123095 (E.T.C.), NIH AG071966 (E.T.C.), NIH AI175317 (E.T.C.), The Smith Family Foundation (E.T.C.), the American Federation for Aging Research (E.T.C.), The Dana-Farber Cancer Institute Innovation Research Fund (E.T.C.). E.T.C. is an HHMI Investigator. The authors thank M. Cameron for assessing *in vitro* hepatic microsomal stability of SCAs. Cartoon illustrations in Figures 1a,g, 2b,c and 5h were created with BioRender.com.

Competing Interests

E.T.C. is co-founder of Matchpoint Therapeutics and Aevum Therapeutics. J.C. is a co-founder of Matchpoint Therapeutics, scientific co-founder of M3 Bioinformatics & Technology Inc., and consultant and equity holder for Soltego and Allorion. N.S.G. is a founder, science advisory board member (SAB) and equity holder in Syros, C4, Allorion, Lighthorse, Inception, Matchpoint, Shenandoah (board member), Larkspur (board member) and Soltego (board member). The Gray lab receives or has received research funding from Novartis, Takeda, Astellas, Taiho, Jansen, Kinogen, Arbella, Deerfield, Springworks, Interline and Sanofi. M.Y.N., E.T.C., J.C., T.Z. and N.S.G. have filed patent for the compounds described in this work. All other authors declare no competing interests.

Author Contributions

M.Y.N., J.C., T.Z., N.S.G. and E.T.C. conceived of and designed the study. M.Y.N. performed cellular experiments and analyzed data. M.N.N., G.D., I.D., S.T., J.C. and T.Z. designed and conducted chemical syntheses. M.Y.N., N.B. and S.W. developed and designed OxImmune resource and web application. H.X.

provided Oximouse dataset. M.Y.N., S.S. and H.X. carried out and analyzed data from CPT mass spectrometry experiments. H.X. developed CPT-MS technology. M.Y.N. and S.S. carried out and analyzed data from SHP1 intact protein and SHP1 cysteine site engagement mass spectrometry experiments. H.-S.S. and S.D.-P. carried out and oversaw SHP1 proteins expression and purification. J.C. performed molecular modeling. M.Y.N., T.W. and J.E. designed and carried out HDX mass spectrometry experiments and analyzed data. M.Y.N. and E.L.M. performed and analyzed data from *in vivo* experiments. J.C., T.Z., N.S.G. and E.T.C. directed the research, oversaw the experiments, and wrote the manuscript with assistance from the other authors.

1 O'Neill, L. A. & Pearce, E. J. Immunometabolism governs dendritic cell and macrophage function. *J Exp Med* **213**, 15-23 (2016). https://doi.org/10.1084/jem.20151570

2 Tran, N. & Mills, E. L. Redox regulation of macrophages. *Redox Biol* **72**, 103123 (2024). https://doi.org/10.1016/j.redox.2024.103123

3 Lennicke, C. & Cochemé, H. M. Redox metabolism: ROS as specific molecular regulators of cell signaling and function. *Molecular Cell* **81**, 3691-3707 (2021). https://doi.org/10.1016/j.molcel.2021.08.018

4 Schieber, M. & Chandel, N. S. ROS function in redox signaling and oxidative stress. *Curr Biol* **24**, R453-R462 (2014). https://doi.org/10.1016/j.cub.2014.03.034

5 West, A. P., Shadel, G. S. & Ghosh, S. Mitochondria in innate immune responses. *Nat Rev Immunol* **11**, 389-402 (2011). https://doi.org/10.1038/nri2975

6 Murphy, M. P. & O'Neill, L. A. J. Krebs Cycle Reimagined: The Emerging Roles of Succinate and Itaconate as Signal Transducers. *Cell* **174**, 780-784 (2018). https://doi.org/10.1016/j.cell.2018.07.030

7 Mills, E. L. *et al.* Succinate Dehydrogenase Supports Metabolic Repurposing of Mitochondria to Drive Inflammatory Macrophages. *Cell* **167**, 457-470 e413 (2016). https://doi.org/10.1016/j.cell.2016.08.064

8 Garaude, J. *et al.* Mitochondrial respiratory-chain adaptations in macrophages contribute to antibacterial host defense. *Nat Immunol* **17**, 1037-1045 (2016). https://doi.org/10.1038/ni.3509

9 Mills, E. L. *et al.* Itaconate is an anti-inflammatory metabolite that activates Nrf2 via alkylation of KEAP1. *Nature* **556**, 113-117 (2018). https://doi.org/10.1038/nature25986

10 Bambouskova, M. *et al.* Electrophilic properties of itaconate and derivatives regulate the IκBζ-ATF3 inflammatory axis. *Nature* **556**, 501-504 (2018). https://doi.org/10.1038/s41586-018-0052-z

11 Vinogradova, E. V. *et al.* An Activity-Guided Map of Electrophile-Cysteine Interactions in Primary Human T Cells. *Cell* **182**, 1009-1026.e29 (2020). https://doi.org/10.1016/j.cell.2020.07.001

12 Boike, L., Henning, N. J. & Nomura, D. K. Advances in covalent drug discovery. *Nature Reviews Drug Discovery* **21**, 881-898 (2022). https://doi.org/10.1038/s41573-022-00542-z

13 Weerapana, E. *et al.* Quantitative reactivity profiling predicts functional cysteines in proteomes. *Nature* **468**, 790-795 (2010). https://doi.org/10.1038/nature09472

14 Xiao, H. *et al.* A Quantitative Tissue-Specific Landscape of Protein Redox Regulation during Aging. *Cell* **180**, 968-983 e924 (2020). https://doi.org/10.1016/j.cell.2020.02.012

15 Kisty, E. A., Saart, E. C. & Weerapana, E. Identifying Redox-Sensitive Cysteine Residues in Mitochondria. *Antioxidants (Basel)* **12**, 992 (2023). https://doi.org/10.3390/antiox12050992

16 Carroll, K. Defining and refining the cysteine redoxome with sulfur chemical biology. *ChemRxiv* [Preprint] (2022). https://doi.org/10.26434/chemrxiv-2022-pmk47

17 Breuer, K. *et al.* InnateDB: systems biology of innate immunity and beyond--recent updates and continuing curation. *Nucleic Acids Res* **41**, D1228-1233 (2013). https://doi.org/10.1093/nar/gks1147

18 Fu, L. *et al.* Nucleophilic covalent ligand discovery for the cysteine redoxome. *Nat Chem Biol* **19**, 1309-1319 (2023). http://doi.org/10.1038/s41589-023-01330-5

19 Scheer, J. M., Romanowski, M. J. & Wells, J. A. A common allosteric site and mechanism in caspases. *Proc Natl Acad Sci U S A* **103**, 7595-600 (2006). https://doi.org/10.1073/pnas.0602571103

20 Bozonet, S. M. *et al.* Oxidation of caspase-8 by hypothiocyanous acid enables TNF-mediated necroptosis. *J Biol Chem* **299**, 104792 (2023). https://doi.org/10.1016/j.jbc.2023.104792

21 Yang, J. *et al.* Mechanism of gasdermin D recognition by inflammatory caspases and their inhibition by a gasdermin D-derived peptide inhibitor. *Proc Natl Acad Sci U S A* **115**, 6792-6797 (2018). https://doi.org/10.1073/pnas.1800562115

22 Brady, K. D. *et al.* A catalytic mechanism for caspase-1 and for bimodal inhibition of caspase-1 by activated aspartic ketones. *Bioorg Med Chem* **7**, 621-631 (1999). https://doi.org/10.1016/s0968-0896(99)00009-7
23 Xu, J. H. *et al.* Integrative X-ray Structure and Molecular Modeling for the Rationalization of Procaspase-8 Inhibitor Potency and Selectivity. *ACS Chem Biol* **15**, 575-586 (2020). https://doi.org/10.1021/acschembio.0c00019
24 Xu, G. *et al.* Covalent inhibition revealed by the crystal structure of the caspase-8/p35 complex. *Nature* **410**, 494-497 (2001). https://doi.org/10.1038/35068604
25 Wang, Z. *et al.* Kinetic and structural characterization of caspase-3 and caspase-8 inhibition by a novel class of irreversible inhibitors. *Biochim Biophys Acta* **1804**, 1817-1831 (2010). https://doi.org/10.1016/j.bbapap.2010.05.007
26 Smith, J. K. *et al.* Identification of a redox-sensitive switch within the JAK2 catalytic domain. *Free Radic Biol Med* **52**, 1101-1110 (2012). https://doi.org/10.1016/j.freeradbiomed.2011.12.025
27 Truong, T. H. & Carroll, K. S. Redox regulation of protein kinases. *Crit Rev Biochem Mol Biol* **48**, 332-356 (2013). https://doi.org/10.3109/10409238.2013.790873
28 Castelo-Soccio, L. *et al.* Protein kinases: drug targets for immunological disorders. *Nat Rev Immunol* **23**, 787-806 (2023). https://doi.org/10.1038/s41577-023-00877-7 Erratum in: *Nat Rev Immunol* **24**, 79 (2024). https://doi.org/10.1038/s41577-023-00976-5
29 Ghoreschi, K., Laurence, A. & O'Shea, J. J. Janus kinases in immune cell signaling. *Immunol Rev* **228**, 273-287 (2009). https://doi.org/10.1111/j.1600-065X.2008.00754.x
30 Singh, S. *et al.* The reduced activity of PP-1α under redox stress condition is a consequence of GSH-mediated transient disulfide formation. *Sci Rep* **8**, 17711 (2018). https://doi.org/10.1038/s41598-018-36267-6
31 Chu, Y. *et al.* Effect of activation of protein phosphatase 1 on sulfhydryl reactivity. *Arch Biochem Biophys* **334**, 83-88 (1996). https://doi.org/10.1006/abbi.1996.0432
32 Kim, H. S. *et al.* Constitutive induction of p-Erk1/2 accompanied by reduced activities of protein phosphatases 1 and 2A and MKP3 due to reactive oxygen species during cellular senescence. *J Biol Chem* **278**, 37497-37510 (2003). https://doi.org/10.1074/jbc.M211739200
33 Visscher, M., Arkin, M. R. & Dansen, T. B. Covalent targeting of acquired cysteines in cancer. *Current opinion in chemical biology* **30**, 61-67 (2016). https://doi.org/10.1016/j.cbpa.2015.11.004
34 Shannon, D. A. & Weerapana, E. Covalent protein modification: the current landscape of residue-specific electrophiles. *Current opinion in chemical biology* **24**, 18-26 (2015). https://doi.org/10.1016/j.cbpa.2014.10.021
35 Stanford, S. M. & Bottini, N. Targeting protein phosphatases in cancer immunotherapy and autoimmune disorders. *Nature Reviews Drug Discovery* **22**, 273-294 (2023). https://doi.org/10.1038/s41573-022-00618-w
36 Nandan, D. & Reiner, N. E. Leishmania donovani engages in regulatory interference by targeting macrophage protein tyrosine phosphatase SHP-1. *Clin Immunol* **114**, 266-277 (2005). https://doi.org/10.1016/j.clim.2004.07.017
37 Croker, B. A. *et al.* Inflammation and autoimmunity caused by a SHP1 mutation depend on IL-1, MyD88, and a microbial trigger. *Proc Natl Acad Sci U S A* **105**, 15028-15033 (2008). https://doi.org/10.1073/pnas.0806619105
38 Singh, K. *et al.* ERK-dependent T cell receptor threshold calibration in rheumatoid arthritis. *J Immunol* **183**, 8258-8267 (2009). https://doi.org/10.4049/jimmunol.0901784
39 Christophi, G. P. *et al.* Interferon-beta treatment in multiple sclerosis attenuates inflammatory gene expression through inducible activity of the phosphatase SHP-1. *Clin Immunol* **133**, 27-44 (2009). https://doi.org/10.1016/j.clim.2009.05.019
40 Christophi, G. P. *et al.* Macrophages of multiple sclerosis patients display deficient SHP-1 expression and enhanced inflammatory phenotype. *Lab Invest* **89**, 742-759 (2009). https://doi.org/10.1038/labinvest.2009.32

41 Markovics, A., Toth, D. M., Glant, T. T. & Mikecz, K. Regulation of autoimmune arthritis by the SHP-1 tyrosine phosphatase. *Arthritis Research & Therapy* **22**, 160 (2020). https://doi.org/10.1186/s13075-020-02250-8
42 An, H. *et al.* Phosphatase SHP-1 promotes TLR- and RIG-I-activated production of type I interferon by inhibiting the kinase IRAK1. *Nature Immunology* **9**, 542-550 (2008). https://doi.org/10.1038/ni.1604
43 Abram, C. L. & Lowell, C. A. Shp1 function in myeloid cells. *J Leukoc Biol* **102**, 657-675 (2017). https://doi.org/10.1189/jlb.2MR0317-105R
44 Wang, W. *et al.* Crystal Structure of Human Protein Tyrosine Phosphatase SHP-1 in the Open Conformation. *J Cell Biochem* **112**, 2062-2071 (2011). https://doi.org/10.1002/jcb.23125
45 Darabedian, N. *et al.* Depletion of creatine phosphagen energetics with a covalent creatine kinase inhibitor. *Nat Chem Biol* **19**, 815-824 (2023). https://doi.org/10.1038/s41589-023-01273-x
46 Burger, N. *et al.* A comprehensive landscape of the zinc-regulated human proteome. *bioRxiv* [Preprint] 2024.01.04.574225 (2024). https://doi.org/10.1101/2024.01.04.574225
47 Yang, F. et al. IKK beta plays an essential role in the phosphorylation of RelA/p65 on serine 536 induced by lipopolysaccharide. *J Immunol* **170**, 5630-5635 (2003). https://doi.org/10.4049/jimmunol.170.11.5630
48 Lorenz, U. SHP-1 and SHP-2 in T cells: two phosphatases functioning at many levels. *Immunol Rev* **228**, 342-359 (2009). https://doi.org/10.1111/j.1600-065X.2008.00760.x
49 Pao, L. I. *et al.* Nonreceptor protein-tyrosine phosphatases in immune cell signaling. *Annu Rev Immunol* **25**, 473-523 (2007). https://doi.org/10.1146/annurev.immunol.23.021704.115647
50 Bodenhofer, U. *et al.* msa: an R package for multiple sequence alignment. *Bioinformatics* **31**, 3997-3999 (2015). https://doi.org/10.1093/bioinformatics/btv494
51 Damle, N. P. & Köhn, M. The human DEPhOsphorylation Database DEPOD: 2019 update. *Database (Oxford)* **2019**, baz133 (2019). https://doi.org/10.1093/database/baz133
52 Hu, R. *et al.* KinaseMD: kinase mutations and drug response database. *Nucleic Acids Res* **49**, D552-561 (2021). https://doi.org/10.1093/nar/gkaa945
53 Uhlén, M. *et al.* Proteomics. Tissue-based map of the human proteome. *Science* **347**, 1260419 (2015). https://doi.org/10.1126/science.1260419
54 Liska, O. *et al.* TFLink: an integrated gateway to access transcription factor-target gene interactions for multiple species. *Database (Oxford)* **2022**, baac083 (2022). https://doi.org/10.1093/database/baac083
55 Corcoran, C. C. *et al.* From 20th century metabolic wall charts to 21st century systems biology: database of mammalian metabolic enzymes. *Am J Physiol Renal Physiol* **312**, F533-542 (2017). https://doi.org/10.1152/ajprenal.00601.2016
56 Evavold, C. L. *et al.* Control of gasdermin D oligomerization and pyroptosis by the Ragulator-Rag-mTORC1 pathway. *Cell* **184**, 4495-4511.e19. (2021). https://doi.org/10.1016/j.cell.2021.06.028
57 Eng, J. K., Jahan, T. A. & Hoopmann, M. R. Comet: an open-source MS/MS sequence database search tool. *Proteomics* **13**, 22-24 (2013). https://doi.org/10.1002/pmic.201200439
58 Wales, T. E. & Engen, J. R. Hydrogen exchange mass spectrometry for the analysis of protein dynamics. *Mass Spectrom Rev* **25**, 158-170 (2006). https://doi.org/10.1002/mas.20064

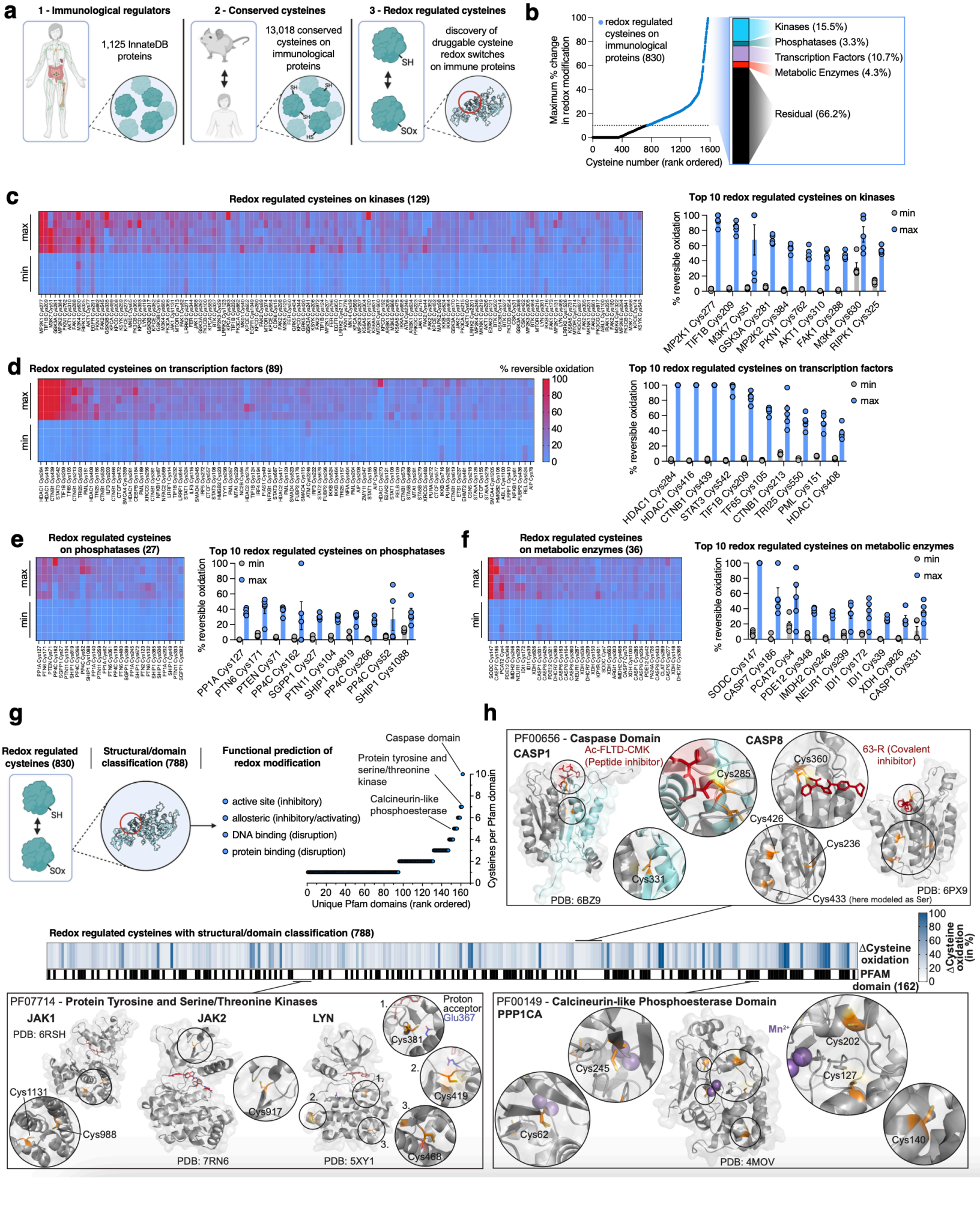
a
1 - Immunological regulators
1,125 InnateDB proteins
2 - Conserved cysteines
13,018 conserved cysteines on immunological proteins
3 - Redox regulated cysteines
discovery of druggable cysteine redox switches on immune proteins
SH
SOx
b
redox regulated cysteines on immunological proteins (830)
Maximum % change in redox modification
Cysteine number (rank ordered)
Kinases (15.5%)
Phosphatases (3.3%)
Transcription Factors (10.7%)
Metabolic Enzymes (4.3%)
Residual (66.2%)
c
Redox regulated cysteines on kinases (129)
max
min
Top 10 redox regulated cysteines on kinases
% reversible oxidation
MP2K1 Cys277
TIF1B Cys209
M3K7 Cys51
GSK3A Cys281
MP2K2 Cys384
PKN1 Cys762
AKT1 Cys310
FAK1 Cys288
M3K4 Cys630
RIPK1 Cys325
d
Redox regulated cysteines on transcription factors (89)
% reversible oxidation
Top 10 redox regulated cysteines on transcription factors
HDAC1 Cys284
HDAC1 Cys416
CTNB1 Cys439
STAT3 Cys542
TIF1B Cys209
TF65 Cys105
CTNB1 Cys213
TRI25 Cys550
PML Cys151
HDAC1 Cys408
e
Redox regulated cysteines on phosphatases (27)
Top 10 redox regulated cysteines on phosphatases
PP1A Cys127
PTN6 Cys171
PTEN Cys71
PP4C Cys162
SGPP1 Cys27
PTN11 Cys104
SHIP1 Cys819
PP4C Cys266
PP4C Cys52
SHIP1 Cys1088
f
Redox regulated cysteines on metabolic enzymes (36)
Top 10 redox regulated cysteines on metabolic enzymes
SODC Cys147
CASP7 Cys186
PCAT2 Cys4
PDE12 Cys348
IMDH2 Cys246
NEUR1 Cys299
IDI1 Cys172
IDI1 Cys39
XDH Cys826
CASP1 Cys331
g
Redox regulated cysteines (830)
Structural/domain classification (788)
Functional prediction of redox modification
active site (inhibitory)
allosteric (inhibitory/activating)
DNA binding (disruption)
protein binding (disruption)
Caspase domain
Protein tyrosine and serine/threonine kinase
Calcineurin-like phosphoesterase
Cysteines per Pfam domain
Unique Pfam domains (rank ordered)
h
PF00656 - Caspase Domain
CASP1
Ac-FLTD-CMK (Peptide inhibitor)
CASP8
63-R (Covalent inhibitor)
Cys285
Cys360
Cys426
Cys236
Cys331
Cys433 (here modeled as Ser)
PDB: 6BZ9
PDB: 6PX9
Redox regulated cysteines with structural/domain classification (788)
ΔCysteine oxidation
PFAM domain (162)
ΔCysteine oxidation (in %)
PF07714 - Protein Tyrosine and Serine/Threonine Kinases
JAK1
PDB: 6RSH
JAK2
LYN
Proton acceptor Glu367
Cys1131
Cys988
Cys917
Cys381
Cys419
Cys468
PDB: 7RN6
PDB: 5XY1
PF00149 - Calcineurin-like Phosphoesterase Domain
PPP1CA
Mn2+
Cys245
Cys202
Cys127
Cys62
Cys140
PDB: 4MOV

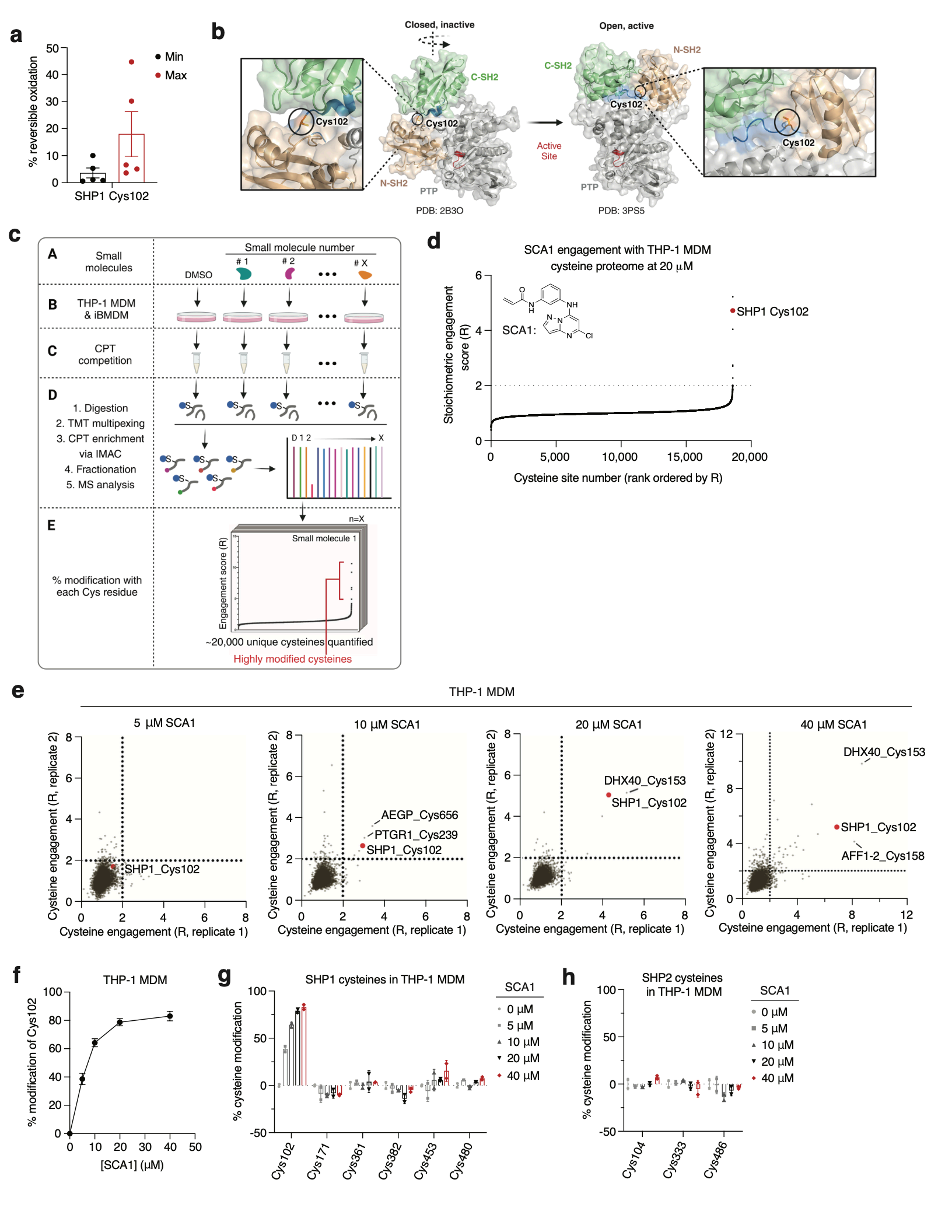
a
% reversible oxidation
Min
Max
SHP1 Cys102
b
Closed, inactive
Open, active
C-SH2
N-SH2
Cys102
Active Site
PTP
PDB: 2B3O
PDB: 3PS5
c
Small molecule number
DMSO
1
2
X
A Small molecules
B THP-1 MDM & iBMDM
C CPT competition
D
1. Digestion
2. TMT multipexing
3. CPT enrichment via IMAC
4. Fractionation
5. MS analysis
E
% modification with each Cys residue
n=X
Small molecule 1
Engagement score (R)
~20,000 unique cysteines quantified
Highly modified cysteines
d
SCA1 engagement with THP-1 MDM cysteine proteome at 20 μM
SCA1:
SHP1 Cys102
Stoichiometric engagement score (R)
Cysteine site number (rank ordered by R)
e
THP-1 MDM
5 μM SCA1
10 μM SCA1
20 μM SCA1
40 μM SCA1
Cysteine engagement (R, replicate 2)
Cysteine engagement (R, replicate 1)
SHP1_Cys102
AEGP_Cys656
PTGR1_Cys239
DHX40_Cys153
AFF1-2_Cys158
f
THP-1 MDM
% modification of Cys102
[SCA1] (μM)
g
SHP1 cysteines in THP-1 MDM
% cysteine modification
SCA1
0 μM
5 μM
10 μM
20 μM
40 μM
Cys102
Cys171
Cys361
Cys382
Cys453
Cys480
h
SHP2 cysteines in THP-1 MDM
Cys104
Cys333
Cys486

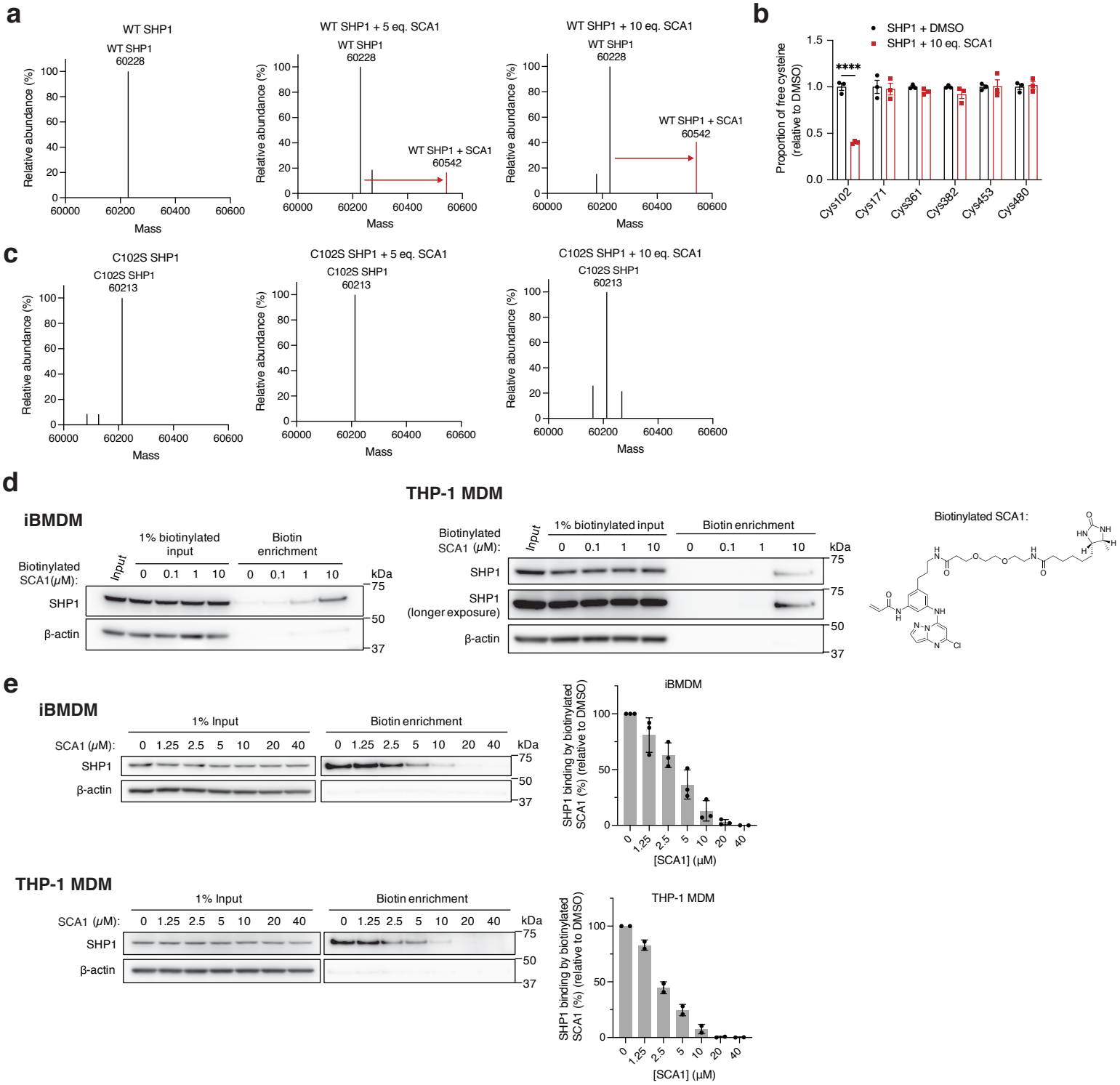
a
WT SHP1
WT SHP1
60228
WT SHP1 + 5 eq. SCA1
WT SHP1 + SCA1
60542
WT SHP1 + 10 eq. SCA1
Relative abundance (%)
Mass
b
SHP1 + DMSO
SHP1 + 10 eq. SCA1
Proportion of free cysteine (relative to DMSO)
****
Cys102
Cys171
Cys361
Cys382
Cys453
Cys480
c
C102S SHP1
C102S SHP1
60213
C102S SHP1 + 5 eq. SCA1
C102S SHP1 + 10 eq. SCA1
d
iBMDM
THP-1 MDM
1% biotinylated input
Biotin enrichment
Biotinylated SCA1 (μM):
Input
SHP1
SHP1 (longer exposure)
β-actin
kDa
Biotinylated SCA1:
e
iBMDM
THP-1 MDM
1% Input
Biotin enrichment
SCA1 (μM):
SHP1 binding by biotinylated SCA1 (%) (relative to DMSO)
[SCA1] (μM)

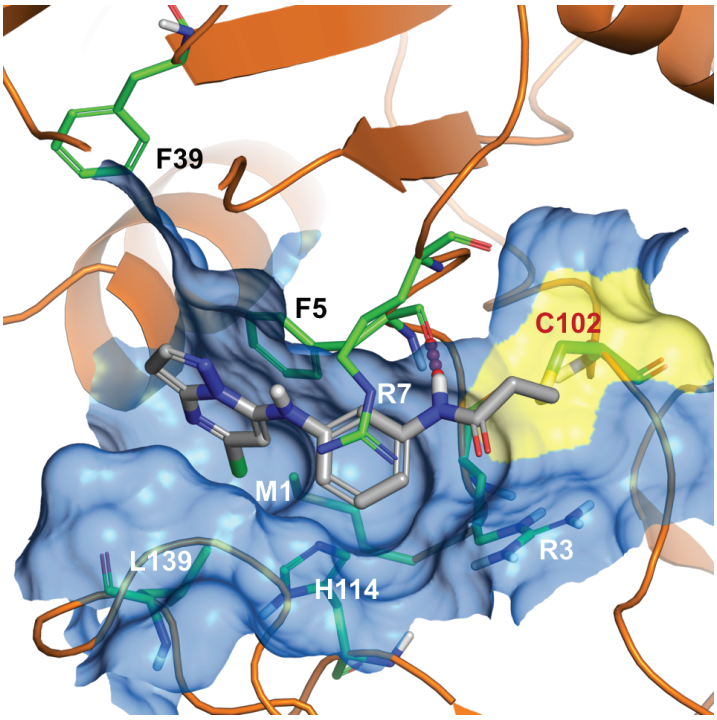

b

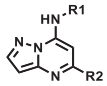

Compound ID	R1	R2	% labeling	Compound ID	R1	R2	% labeling
SCA1		Cl	46.3	SCA10		Cl	0
SCA2		Cl	0	SCA11		Cl	0
SCA3		Cl	0	SCA12		H	0
SCA4		Cl	0	SCA13		NH2	10.4
SCA5		Cl	29.6	SCA14		NMe2	0
SCA6		Cl	37.1	SCA15		OMe	31.9
SCA7		Cl	100	SCA16			0
SCA8		Cl	20.9	SCA17			0
SCA9		Cl	100				

c

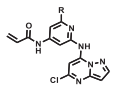

Compound ID	R	% labeling
SCA18		70.7
SCA19		13.8
SCA20		54.1
SCA21		47.5
SCA22		25
SCA23		24
SCA24		0
SCA25	F	100
SCA26		0

d

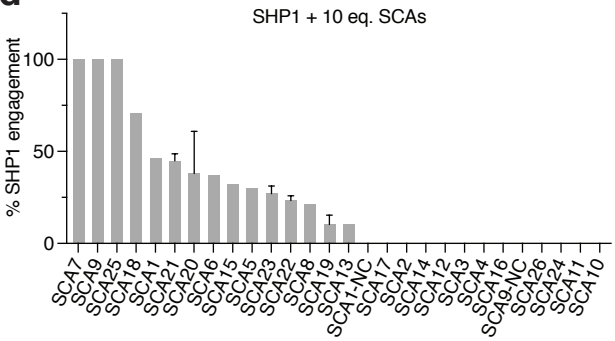

e

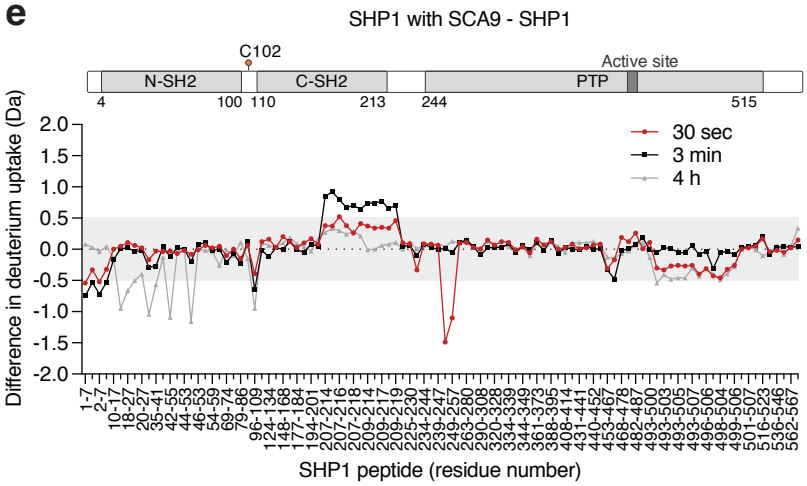

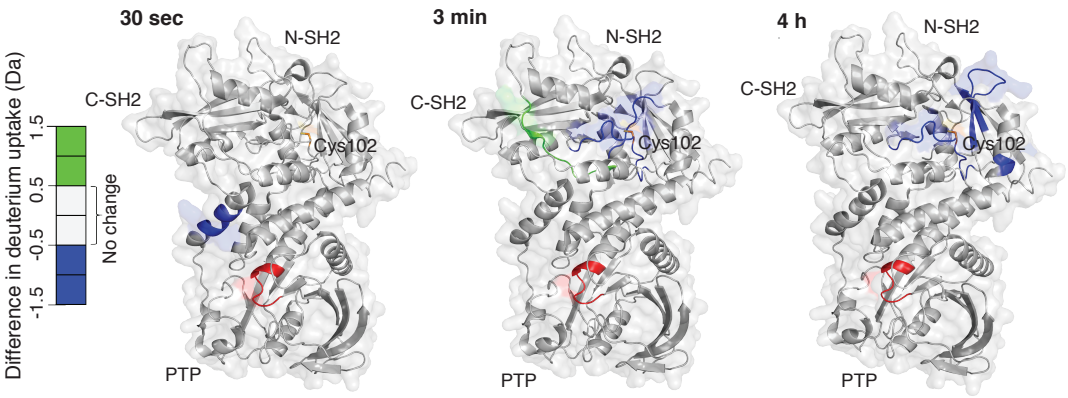

f

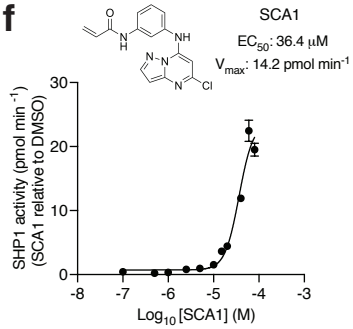

g

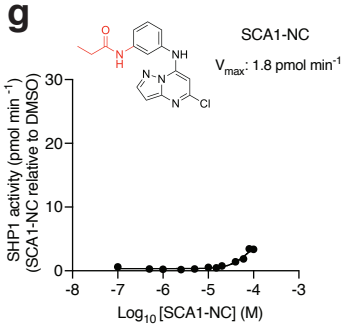

h

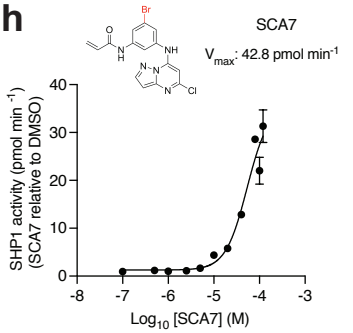

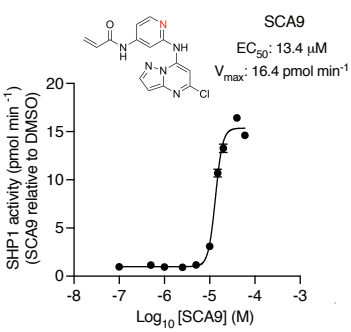

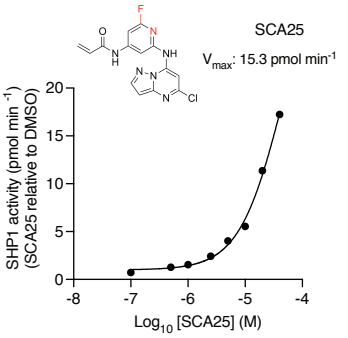

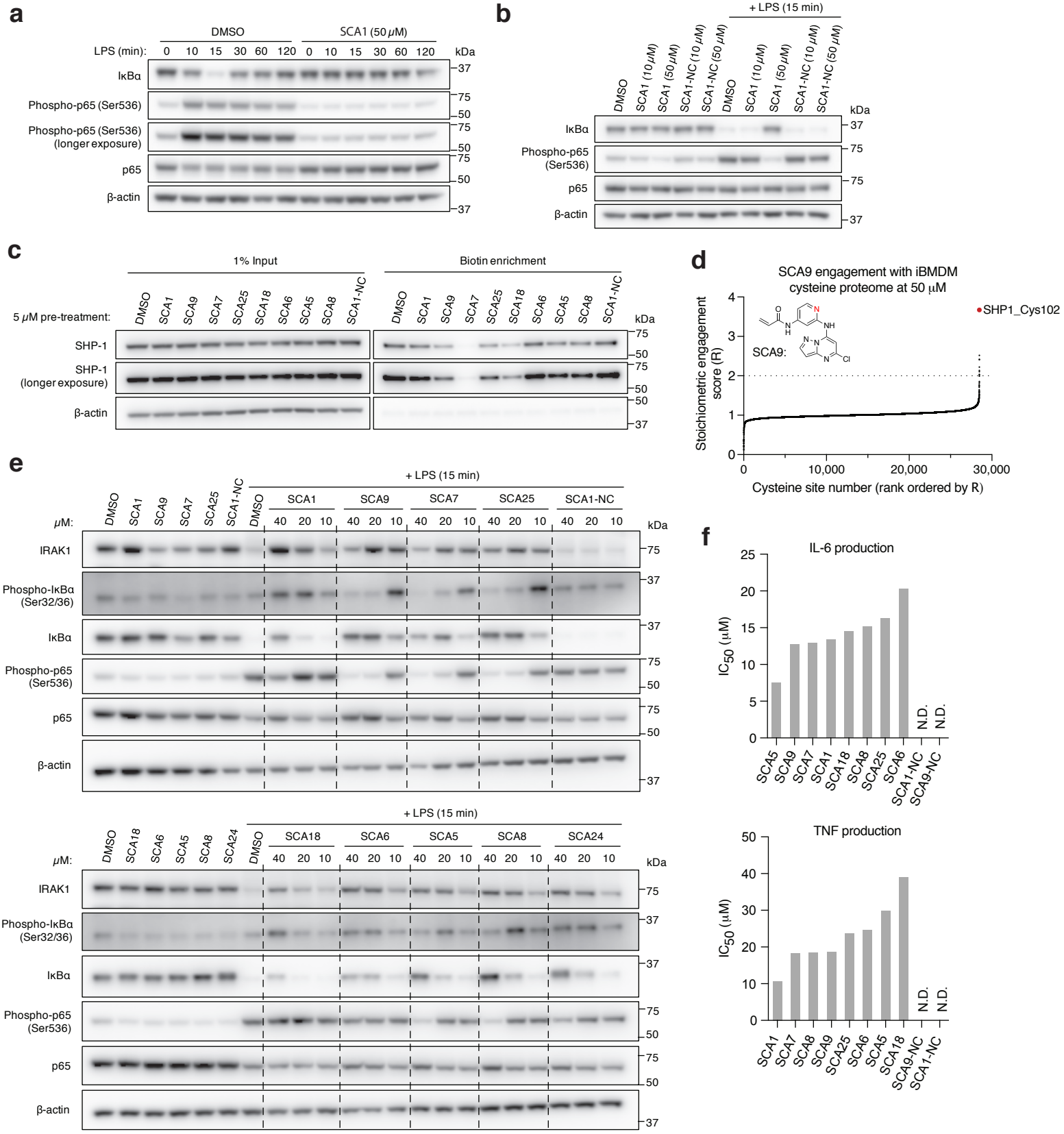
a
DMSO
SCA1 (50 μM)
LPS (min): 0 10 15 30 60 120 0 10 15 30 60 120
kDa
IκBα
Phospho-p65 (Ser536)
Phospho-p65 (Ser536) (longer exposure)
p65
β-actin
b
+ LPS (15 min)
DMSO
SCA1 (10 μM)
SCA1 (50 μM)
SCA1-NC (10 μM)
SCA1-NC (50 μM)
IκBα
Phospho-p65 (Ser536)
p65
β-actin
c
1% Input
Biotin enrichment
5 μM pre-treatment:
DMSO SCA1 SCA9 SCA7 SCA25 SCA18 SCA6 SCA5 SCA8 SCA1-NC
SHP-1
SHP-1 (longer exposure)
β-actin
d
SCA9 engagement with iBMDM cysteine proteome at 50 μM
SHP1_Cys102
SCA9:
Stoichiometric engagement score (R)
Cysteine site number (rank ordered by R)
e
+ LPS (15 min)
μM:
SCA1 SCA9 SCA7 SCA25 SCA1-NC
40 20 10
IRAK1
Phospho-IκBα (Ser32/36)
IκBα
Phospho-p65 (Ser536)
p65
β-actin
SCA18 SCA6 SCA5 SCA8 SCA24
f
IL-6 production
IC50 (μM)
SCA5 SCA9 SCA7 SCA1 SCA18 SCA8 SCA25 SCA6 SCA1-NC SCA9-NC
N.D.
TNF production
SCA1 SCA7 SCA8 SCA9 SCA25 SCA6 SCA5 SCA18 SCA9-NC SCA1-NC

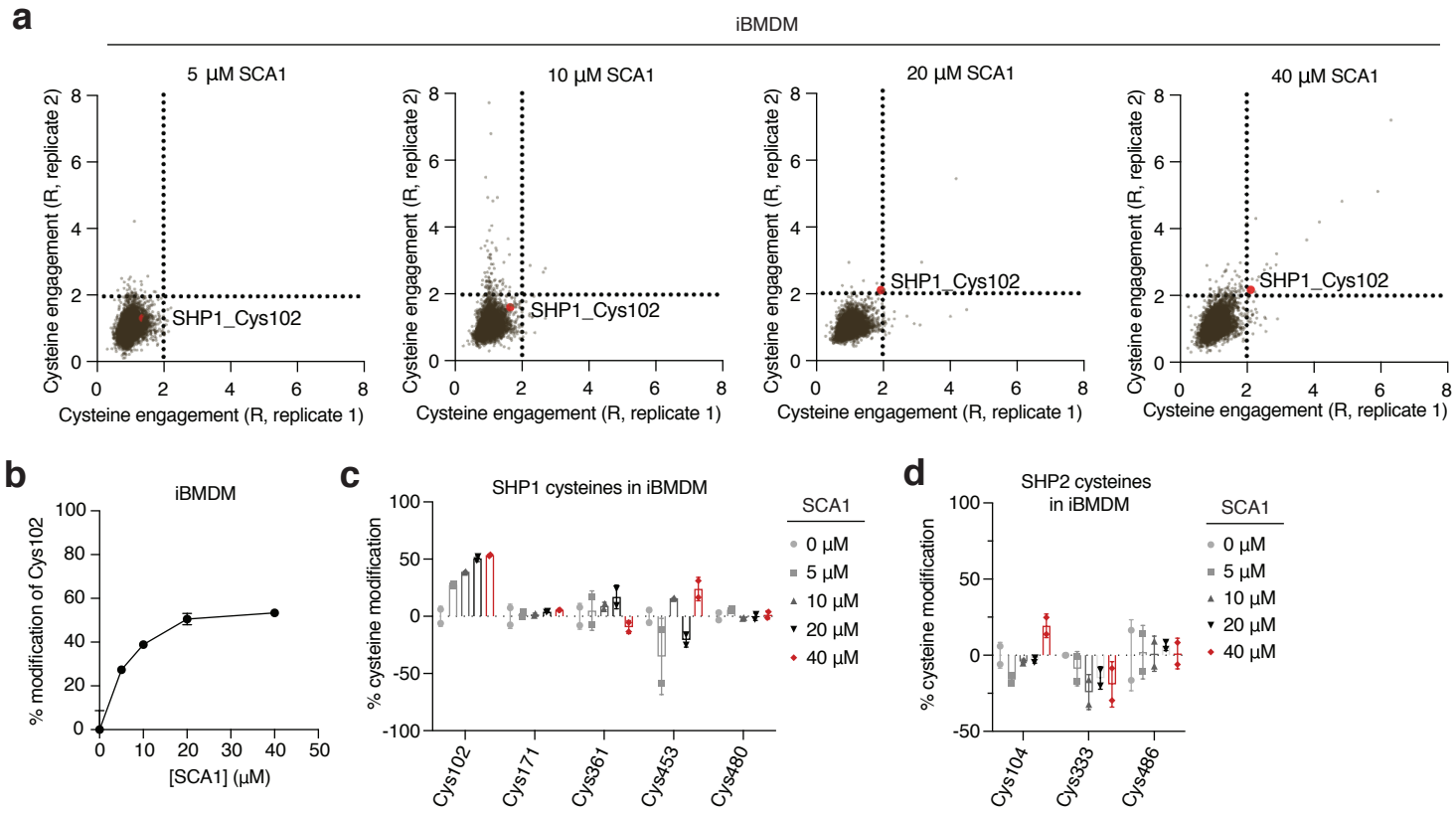
a
iBMDM
5 μM SCA1
10 μM SCA1
20 μM SCA1
40 μM SCA1
Cysteine engagement (R, replicate 2)
Cysteine engagement (R, replicate 1)
SHP1_Cys102
b
iBMDM
% modification of Cys102
[SCA1] (μM)
c
SHP1 cysteines in iBMDM
% cysteine modification
Cys102
Cys171
Cys361
Cys453
Cys480
SCA1
0 μM
5 μM
10 μM
20 μM
40 μM
d
SHP2 cysteines in iBMDM
% cysteine modification
Cys104
Cys333
Cys486
SCA1
0 μM
5 μM
10 μM
20 μM
40 μM

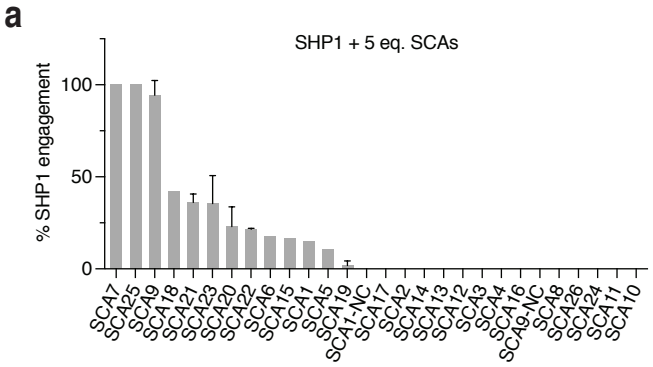
a
SHP1 + 5 eq. SCAs
% SHP1 engagement
100
50
0
SCA7
SCA25
SCA9
SCA18
SCA21
SCA23
SCA20
SCA22
SCA6
SCA15
SCA1
SCA5
SCA19
SCA1-NC
SCA17
SCA2
SCA14
SCA13
SCA12
SCA3
SCA4
SCA16
SCA9-NC
SCA8
SCA26
SCA24
SCA11
SCA10

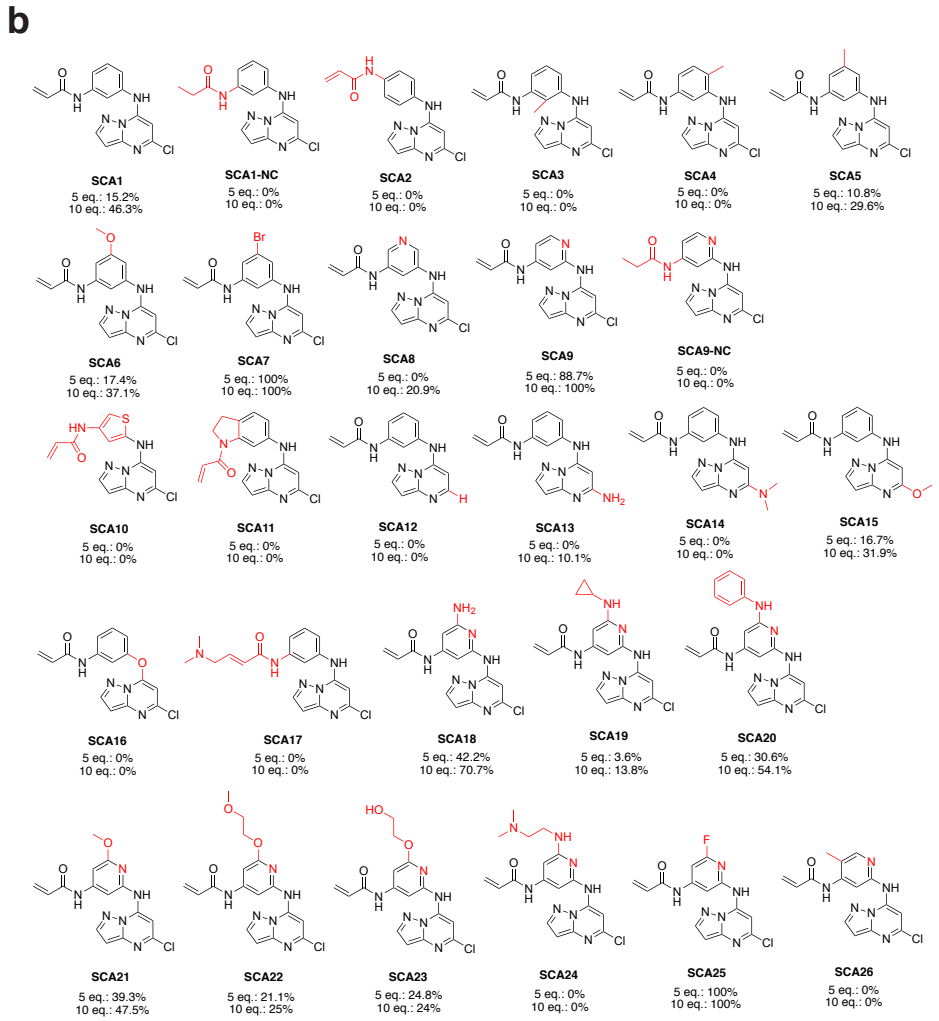
b
SCA1
5 eq.: 15.2%
10 eq.: 46.3%
SCA1-NC
5 eq.: 0%
10 eq.: 0%
SCA2
5 eq.: 0%
10 eq.: 0%
SCA3
5 eq.: 0%
10 eq.: 0%
SCA4
5 eq.: 0%
10 eq.: 0%
SCA5
5 eq.: 10.8%
10 eq.: 29.6%
SCA6
5 eq.: 17.4%
10 eq.: 37.1%
SCA7
5 eq.: 100%
10 eq.: 100%
SCA8
5 eq.: 0%
10 eq.: 20.9%
SCA9
5 eq.: 88.7%
10 eq.: 100%
SCA9-NC
5 eq.: 0%
10 eq.: 0%
SCA10
5 eq.: 0%
10 eq.: 0%
SCA11
5 eq.: 0%
10 eq.: 0%
SCA12
5 eq.: 0%
10 eq.: 0%
SCA13
5 eq.: 0%
10 eq.: 10.1%
SCA14
5 eq.: 0%
10 eq.: 0%
SCA15
5 eq.: 16.7%
10 eq.: 31.9%
SCA16
5 eq.: 0%
10 eq.: 0%
SCA17
5 eq.: 0%
10 eq.: 0%
SCA18
5 eq.: 42.2%
10 eq.: 70.7%
SCA19
5 eq.: 3.6%
10 eq.: 13.8%
SCA20
5 eq.: 30.6%
10 eq.: 54.1%
SCA21
5 eq.: 39.3%
10 eq.: 47.5%
SCA22
5 eq.: 21.1%
10 eq.: 25%
SCA23
5 eq.: 24.8%
10 eq.: 24%
SCA24
5 eq.: 0%
10 eq.: 0%
SCA25
5 eq.: 100%
10 eq.: 100%
SCA26
5 eq.: 0%
10 eq.: 0%

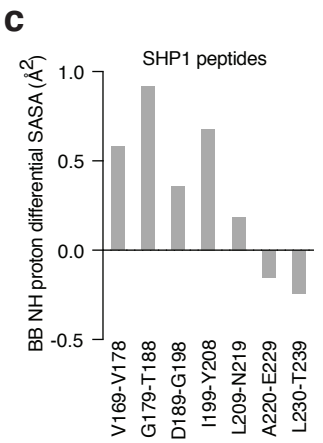
c
SHP1 peptides
BB NH proton differential SASA (Å²)
1.0
0.5
0.0
-0.5
V169-V178
G179-T188
D189-G198
I199-Y208
L209-N219
A220-E229
L230-T239

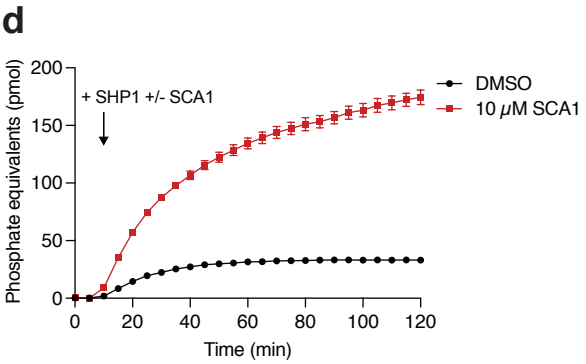
d
Phosphate equivalents (pmol)
200
150
100
50
0
+ SHP1 +/- SCA1
DMSO
10 μM SCA1
0
20
40
60
80
100
120
Time (min)

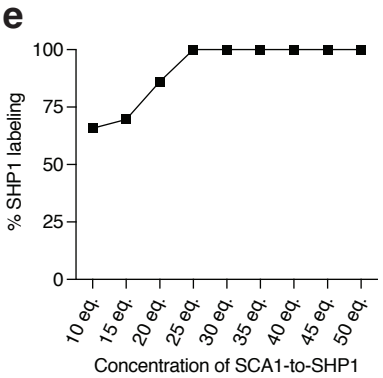
e
% SHP1 labeling
100
75
50
25
0
10 eq.
15 eq.
20 eq.
25 eq.
30 eq.
35 eq.
40 eq.
45 eq.
50 eq.
Concentration of SCA1-to-SHP1

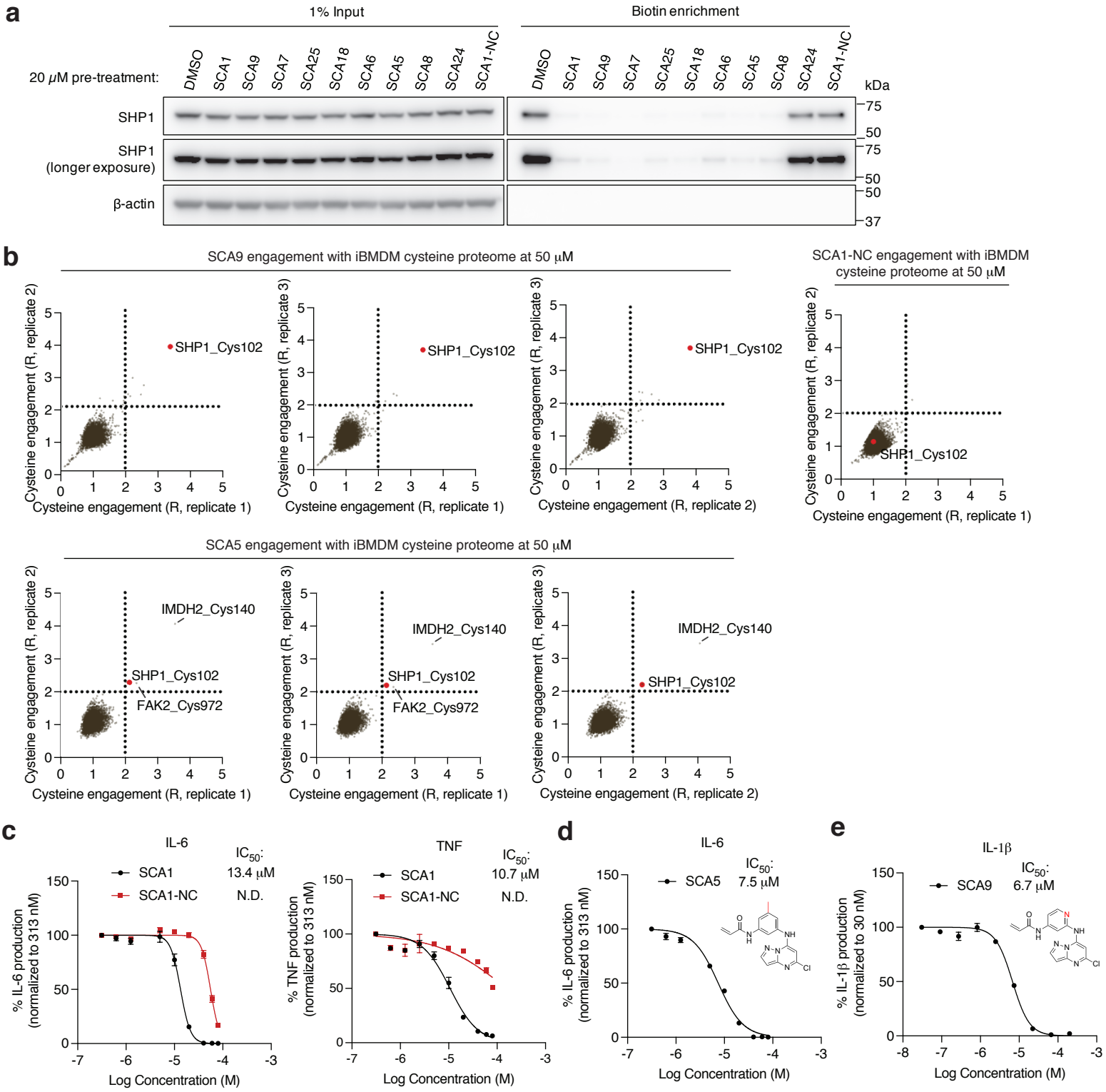
a
1% Input
Biotin enrichment
20 μM pre-treatment:
DMSO
SCA1
SCA9
SCA7
SCA25
SCA18
SCA6
SCA5
SCA8
SCA24
SCA1-NC
kDa
SHP1
SHP1 (longer exposure)
β-actin
75
50
37
b
SCA9 engagement with iBMDM cysteine proteome at 50 μM
SCA1-NC engagement with iBMDM cysteine proteome at 50 μM
SCA5 engagement with iBMDM cysteine proteome at 50 μM
SHP1_Cys102
IMDH2_Cys140
FAK2_Cys972
Cysteine engagement (R, replicate 1)
Cysteine engagement (R, replicate 2)
Cysteine engagement (R, replicate 3)
c
IL-6
SCA1
SCA1-NC
IC50: 13.4 μM
N.D.
% IL-6 production (normalized to 313 nM)
Log Concentration (M)
TNF
IC50: 10.7 μM
% TNF production (normalized to 313 nM)
d
IL-6
SCA5
IC50: 7.5 μM
e
IL-1β
SCA9
IC50: 6.7 μM
% IL-1β production (normalized to 30 nM)